Journal of Materials Chemistry C

Tailoring the Thermoelectric and Structural Properties of Cu-Sn Based Thiospinel Compounds [CuM1+xSn1-xS4 (M = Ti, V, Cr, Co)]

Journal:	*Journal of Materials Chemistry C*
Manuscript ID	TC-ART-09-2020-004393.R2
Article Type:	Paper
Date Submitted by the Author:	05-Nov-2020
Complete List of Authors:	Bourgès, Cédric; National Institute for Materials Science, Thermal Energy Harvesting Group Srinivasan, Bhuvanesh; National Institute for Materials Science Fontaine, Bruno; UMR CNRS 6226 Sciences Chimiques de Rennes , Ecole Nationale Superieure de Chimie de Rennes (ENSCR) Sauerschnig, Philipp; National Institute for Materials Science Minard, Alizee; CNRS-Saint Gobain-NIMS, UMI 3629, Laboratory for Innovative Key Materials and Structures (LINK) Halet, Jean-François; Universite de Rennes 1, Miyazaki, Yuzuru; Tohoku University Berthebaud, David; CNRS-Saint Gobain-NIMS, UMI 3629, Laboratory for Innovative Key Materials and Structures (LINK) Mori, Takao; National Institute for Materials Science,

Tailoring the Thermoelectric and Structural Properties of Cu-Sn Based Thiospinel Compounds [$CuM_{1+x}Sn_{1-x}S_4$ (M = Ti, V, Cr, Co)]

Cédric Bourgès,[1,2] Bhuvanesh Srinivasan,*[1,3] Bruno Fontaine,[4] Philipp Sauerschnig,[1] Alizée Minard,[3] Jean-François Halet,[3,4] Yuzuru Miyazaki,[2] David Berthebaud,[3] and Takao Mori*[1,5]

[1] *WPI International Center for Materials Nanoarchitechtonics (WPI-MANA), National Institute for Materials Science (NIMS), Namiki 1-1, Tsukuba, 305-0044, Japan*

[2] *Department of Applied Physics, Graduate School of Engineering, Tohoku University, Sendai, 980-8579, Japan*

[3] *CNRS-Saint Gobain-NIMS, UMI 3629, Laboratory for Innovative Key Materials and Structures (LINK), National Institute for Materials Science (NIMS), Tsukuba, 305-0044, Japan*

[4] *Univ. Rennes, Ecole Nationale Supérieure de Chimie de Rennes, CNRS, ISCR – UMR 6226, F-35000 Rennes, France*

[5] *Graduate School of Pure and Applied Sciences, University of Tsukuba, Tennodai 1-1-1, Tsukuba 305-8671, Japan*

* Corresponding authors: SRINIVASAN.Bhuvanesh@nims.go.jp (B.S); MORI.Takao@nims.go.jp (T.M)

Abstract

We report here a rich variation of the thermoelectric properties of a series of Cu-Sn based thiospinels of composition $CuM_{1+x}Sn_{1-x}S_4$ upon partial substitution at the Sn-site with a variety of transition elements (M = Ti, V, Cr, Co). The optimized synthesis and processing conditions we used enabled us to realize highly densified and homogeneous compounds. The V-series was found to exhibit the lowest performing thermoelectric properties, whereas Co and Ti substituted compounds showed moderate thermoelectric properties with a maximum figure of merit (zT_{max}) of ~0.02 and ~0.07 at 673 K, respectively. In contrast, the Cr substituted compounds exhibited better thermoelectric performance with zT ~0.2 at 673 K for the composition $CuCr_{1.2}Sn_{0.8}S_4$. Both *p*- and *n*-type compounds were obtained; specifically, the Co and Ti series were found to be *n*-type, and the Cr series was found to be *p*-type. Besides the suppressed thermal transport, the attractive thermoelectric properties with the Cr-series can be attributed to the simultaneous increase of the Seebeck coefficient and electrical conductivity with increasing temperature, thus resulting in an improved power factor. Experimental and DFT theoretical calculations also predict a considerable interaction between the carriers and magnetic moments, contributing to a higher effective mass, thus leading to higher thermopower and power factor for the Cr-series. Computed electronic density of states and band structures, in agreement with the experimental findings, envisaged *n*-type half-metallic character for the $CuTi_{1+x}Sn_{1-x}S_4$ paramagnetic compounds, *n*-type conducting behavior for the $CuCo_{1+x}Sn_{1-x}S_4$ compounds, *p*-type weak half-metallic character for the $CuV_{1+x}Sn_{1-x}S_4$ compounds, and *p*-type semiconducting behavior for the $CuCr_{1+x}Sn_{1-x}S_4$ ferromagnetic compounds. Computation of the electronic transport coefficients using the Boltzmann Transport Equation also suggests a better thermoelectric property, especially the thermopower, for the Cr-series when compared to its Ti/V/Co counterparts.

Keywords: Annealing and Sintering; Crystal structures; Band structure; Thermoelectrics; Thiospinels

1. Introduction

Thermoelectric (TE) materials and devices with their potential to convert waste heat into useful electricity, while also enabling cooling via electricity, postulate the likelihood of an all-solid-state technology for refrigeration, power generation, temperature stability, and control.[1–6] The TE material's performance is quantified by a dimensionless figure of merit, $zT = S^2\sigma T/\kappa$ where σ, S, T and κ are the electrical conductivity, Seebeck coefficient, absolute temperature and total thermal conductivity (sum of the electronic contribution, κ_e, and the lattice contribution, κ_{latt}), respectively.

The other vital consideration in the design of compounds for TE is the cost factor and the availability of constituent elements, especially for the eventual mass-production for industrial applications. Regrettably, most of the high-performance TE materials are composed of expensive, scarce, and/or toxic elements.[7–13] In this aspect, sulfides have emerged as a viable alternative, particularly the copper-based sulfide compounds such as $Cu_{2-x}S$, chalcopyrites, cubanites, colusites, stannoidites, tetrahedrites, high-entropy copper sulfides and other derivatives of these compounds.[14–28] Of late, in this category of economically feasible and environmentally friendly TE compounds, ternary Cu-based thiospinel materials with a general composition of CuM_2S_4 (M = Ti, Cr, Co, *etc*.) have gained some prominence due to their promising crystallographic structural arrangements and appealing thermodynamic, magnetic, electrical and thermal transport behaviors.[29–32] Incidentally, some tellurides with spinel-related structures have also been found lately with relatively high thermoelectric performance.[33,34] Although some attractive themoelectric properties have been reported for thiospinel compounds in the family of the general composition CuM_2S_4, such as $CuCo_2S_4$, $CuTi_2S_4$, $CuCr_2S_4$ and their derivatives (where Co, Ti, Cr are partially substituted for each other),[29–32,35] not much information is available on the thermoelectric properties of Sn-based thiospinel compounds and their derivatives.

The cubic structure of Sn-based thiospinel ($Fd\bar{3}m$; n° 227) compounds are relatively complex (Figure 1) owing to their large cell parameter (a ~10.2 Å) and a significant number of atoms per unit cell (N = 56). The basic structural framework is composed of mixed occupied [$(M/Sn)S_6$] octahedra sharing their edges and [CuS_4] tetrahedra, which are corner-shared with four octahedra, thus forming a 3-D network assembly similar to that of $Cu_2MTi_3S_8$ (M = Mn, Ni) thiospinel compounds.[36] By modifying the octahedral occupancy atoms and/or by optimizing the vacancies in the large unit cell, the electronic band structure can be manipulated to tune their electrical transport properties, as reported in several thiospinel structures.[30,32,37] The stable tetravalent state of Sn renders the quaternary thiospinel charge balance, *i.e*., $Cu^+M^{3+}Sn^{4+}(S^{2-})_4$ for most of the transition metal (M). Padiou *et al*. (1980)[38] reported that these Cu-Sn based thiospinel compounds exhibit a narrow domain of thermodynamic stability. Considering the generic formula $CuM_{1+x}Sn_{1-x}S_4$, the thiospinel phase was known to exist only in the constricted range of ($-0.1 < x < 1$) for M = Ti, ($-0.15 < x < 1$) for M = V, ($-0.2 < x < 1$) for M = Cr and x = -0.5 for M = Co, according to the previous thermodynamic and radius-crystallographic study.[38] However, this general charge balance description is not fully valid in all situations, especially depending to the x content. Indeed, various authors have confirmed in the case of Co-Ti based compounds that the Co^{3+} ion appears, but it tends to reduce in the presence of Cu^+ and Ti^{3+}, leading to a formal charge of Co^{2+} (low spin (LS)).[31,36] This 2+ oxidation

state for Co allows only the stoichiometric composition of $CuCo_{0.5}Sn_{1.5}S_4$ (as per the charge balance $Cu^{+}Co_{0.5}^{2+}Sn_{1.5}^{4+}(S^{2-})_4$) to follow the charge neutrality rule. In the Ti-based compound case, the material follow the general description for $x = 0$ with a charge balance of $Cu^{+}Ti^{3+}Sn^{4+}(S^{2-})_4$. For $x > 0$, the Cu^{2+} and/or Ti^{4+} formation is necessary for keeping the charge neutrality. It appears that the formation of Ti^{4+} is favorable[30] and conducts to the following equilibrium, $Cu^{+}(Ti^{3+})(Ti^{4+})_x(Sn^{4+})_{1-x}(S^{2-})_4$. For the Cr-based compound, the charge balance can be described theoretically as $Cu^{+}Cr^{3+}Sn^{4+}(S^{2-})_4$ for $x = 0$. However, some reports have confirmed the formation of Cr^{4+} for the $x > 0$ composition, according to the magnetic moment expected for a high spin state of Cr, leading to a global charge balance of $Cu^{+}Cr^{3+}(Cr^{4+})_x(Sn^{4+})_{1-x}(S^{2-})_4$.[39,40]

To the best of our knowledge, the thermoeelctric properties have never been investigated on dense samples at a higher temperature range for such Cu-Sn based thiospinel compounds before. This propels the motivation for this work, where a large variety of compositions of $CuM_{1+x}Sn_{1-x}S_4$ (M = Ti, V, Cr, Co) are explored regarding their thermeoelectrtic properties for the first time. In most of these cases, modifications of the structural and magnetic properties *via* processing conditions and electronic band structure engineering are expected to allow for modifications of the transport properties, thus providing avenues for tuning or tailoring of the thermeoelectric properties.[29,31,41,35,42–45] In addition, the Sn-based thiospinel compounds can possess intrinsically lower thermal conductivity due to the large molar mass of Sn, which might enable the promotion of the mass fluctuation effect,[46,47] which we hope to exploit to tune their thermal transport properties. Besides the thermoelectric aspects, this work also sheds some light on the crystallography, magnetic properties together with thermoelectric correlations, electronic band structures and density of states of these $CuM_{1+x}Sn_{1-x}S_4$ (M = Ti, V, Cr, Co) thiospinel compounds.

2. Materials & Methods

2.1 Synthesis

The samples of $CuM_{1+x}Sn_{1-x}S_4$ (M = Ti, V, Cr, Co) were prepared by vacuum sealed-tube processing, followed by extensive annealing and finally consolidation by Spark Plasma Sintering (SPS). In each case, the composition or the x content were carefully chosen based on the work of Padiou *et al*. (1980),[38] where they have reported the optimized content of x to achieve pure thiospinel compounds. Based on the findings from that work, the compositions of $CuV_{1+x}Sn_{1-x}S_4$ ($-0.15 < x < 1$), $CuCo_{1+x}Sn_{1-x}S_4$ ($x = -0.5$), $CuTi_{1+x}Sn_{1-x}S_4$ ($-0.1 < x < 1$) and $CuTi_{1+x}Sn_{1-x}S_4$ ($-0.2 < x < 1$), were synthesized here in a three-step process. Firstly, the stoichiometric mixture of the powder elements was grinded using a mortar and pestle and sealed in evacuated quartz tubes, heated until the synthesis temperature (100 K/h) and soaked at that temperature for 24 h before cooling down to the room temperature at the same rate. The synthesis temperatures varied based on the composition,[38] *i.e.*, 1043 K for $CuV_{1+x}Sn_{1-x}S_4$ series, 943 K for $CuCo_{1+x}Sn_{1-x}S_4$ compound, 943 K for $CuTi_{1+x}Sn_{1-x}S_4$ series and 973 K for $CuCr_{1+x}Sn_{1-x}S_4$ series. Secondly, the obtained powders were then grinded in a mortar and cold-pressed into pellets (uniaxial pressure of ~100 MPa) and evacuated again in the quartz tube for the second annealing of 72 h at the synthesis temperature. This extended annealing process was later found to be crucial in obtaining the single-phase compounds. The annealed pellets were again crushed and sieved down to < 180 μm. Thirdly, the finely sieved powders were then

sintered (SPS-1080 – SPS Syntex Inc.) at the same temperature as that of the synthesis temperature for 30 mins (heating rate ~50 K/h) with an axial pressure of ~60 MPa (10 mm diameter graphite dies were used) in a partial vacuum atmosphere. The sintered pellets were then cut and polished to the required shapes and dimensions for various transport property measurements.

2.2 Powder X-ray diffraction

X-ray powder diffraction (XRD) patterns were recorded at room temperature in the 2θ range of 10^o – 90^o using Rigaku Smart Lab 3 diffractometer (Cu K_α radiation) with a step size of 0.02^o and a scan speed of 2^o/min. Le Bail fitting and the Rietveld refinement were performed using FullProf program included in the WinPLOTR software.[48–50] The shape of the diffraction peaks was modeled using a pseudo-Voigt profile function.[51] Zero-point shift, asymmetry parameters, the atomic positions and lattice parameters were systematically refined, and the background contribution was manually estimated. The *Biso* has been fixed in order to enable a systematic refinement of the atomic occupancies. The mix occupancy of the 16*c* position was set with the Sn and transition metal (M = Co, Ti and Cr) with an initial ratio of 0.5 before being refined for trying to extract a trend of the octahedral site occupancy. The result has been summarized in supplementary information (SI – Table S1). The mixed occupancy of the Cu and the transition metal in the tetrahedral 8*a* site has not been investigated considering the too close *Z* values between the elements (Cu and M).

2.3 Microscopic analysis

Observation of microstructural aspects of samples was performed on the fractured surface of the sintered samples using a Hitachi SU-8000 Scanning Electron Microscope (SEM).

2.4 Electrical and thermal transport measurements

The electrical resistivity and Seebeck coefficient were measured on ~2×2×8 mm^3 bars simultaneously using a commercial (ZEM-2, ADVANCE RIKO Inc.) instrument under a partial pressure of He.

The temperature-dependent thermal diffusivity, D, was measured on graphite coated disc-shaped samples of 10 mm diameter and ~2 mm thickness using the laser flash diffusivity method in LFA-467 Hyperflash (Netzsch). The temperature-dependent heat capacity, C_p, was derived using a standard sample (pyroceram-9060) in LFA-467, which is in good agreement with the Dulong–Petit C_p value. The total thermal conductivity was calculated using the formula, $\kappa = D \times C_p \times \rho$, where ρ is the density of the sample (measured using Archimedes' principle). In some cases, to better understand the thermal transport properties, the contributions from electronic and lattice parts were calculated. The lattice thermal conductivity (κ_{latt}) was estimated from κ by subtracting the electronic contribution (κ_e) *via* the Wiedemann-Franz law, as in the following equation,

$$\kappa_e = L\sigma T \qquad (1)$$

where κ_e is the electronic thermal conductivity, and L is the Lorenz number computed by the condensed version of Single Parabolic Band model with acoustic phonon scattering (SPB-APS),[52] as in the following equation,

$$L = 1.5 + \exp\left[-\frac{|S|}{116}\right] \quad (2)$$

where the Seebeck coefficient (S) is in μVK^{-1}, and Lorenz number (L) is in 10^{-8} $W\Omega K^{-2}$.

The uncertainty in the results for the values of electrical and thermal transport properties was 5% and 7%, respectively, and for the overall zT was 12%. To improve the readability of the figures, the error bars are not shown.

2.5 Magnetic measurements

Zero-field-cooled (ZFC), field-cooled-cooling (FCC), and field-cooled-warming (FCW) magnetization measurements were carried out on powder samples (~20 mg) from 4 to 300 K under 100 and 1 kOe, and 50 kOe just in the case of $CuCo_{0.5}Sn_{1.5}S_4$, using a Magnetic Properties Measurement System (MPMS, Quantum Design).

2.6 Computational procedures

Spin-polarized geometry optimizations of $CuM_{1+x}Sn_{1-x}S_4$ (x = 0 with M = Ti, V, Cr and x = -0.5 with M = Co) were performed using the VASP code based on density functional theory (DFT).[53] Because of the presence of localized *d*-electrons, an additional Hubbard-like term was introduced for V, Co, Ti, and Cr. The simplified Dudarev approach[54] was used with $U_{eff} = U - J = 3.5$ eV for Ti, V, Co, Cu 3*d* orbitals, and 2.5 eV for Cr 3*d* orbitals (U and J are Hubbard and Hund values, respectively).[55] The exchange-correlation interaction was described within the generalized gradient approximation in the parametrization of the Perdew-Burke-Ernzehof (PBE) functional.[56] Projector-augmented wave potentials were used for all atoms.[57] Calculations were performed with cut-off energy of 400 eV. The electronic wave functions were sampled on dense densities in the irreducible Brillouin Zone (BZ) using the Monkhorst-Pack method.[58] Geometry optimizations, including cell parameters and atomic positions, were carried out without any symmetry constraints. For the electronic band structures and the density of states (DOS), the full-potential linearized augmented plane wave (FLAPW) approach was used, as implemented in the WIEN2K code.[59,60] Since GGA exchange-correlation functionals are known to underestimate experimental band gaps, the modified Becke-Johnson (mBJ) functional proposed by Tran and Blaha was utilized.[61] This functional yields band gaps with an accuracy similar to hybrid functional or GW methods but are obtained at a considerably reduced computational effort. A plane wave cut-off corresponding to $R_{MT}K_{max} = 7$ was used. The radial wave functions inside the non-overlapping muffin-tin spheres were expanded up to $l_{max} = 12$. The charge density was Fourier expanded up to $G_{max} = 16$ Å^{-1}. Total energy convergence was achieved with a BZ integration mesh of 500 *k*-points, generating 60 *k*-points in the irreducible BZ. Electronic dispersion curves and DOS were shifted to set the Fermi level to 0 eV arbitrarily.

The effective carrier mass (m^*), derived for each sample using a single parabolic band model,[62,63] was calculated using the measured room temperature Seebeck coefficient (S) and the computed carrier concentration (n). For the purpose of a qualitative comparison,SI the chemical potential (μ) was estimated using equation (3) with a scattering parameter $\lambda = 0$ (assuming that acoustic-phonon scattering predominates), and where $F_j(\mu)$ are the Fermi integrals given by equation (4). The effective carrier mass can then be determined from equation (5).

$$S = \frac{k_B}{e}\left\{\frac{(2+\lambda)F_{1+\lambda}(\mu)}{(1+\lambda)F_{\lambda}(\mu)} - \mu\right\} \quad (3)$$

$$F_j(\mu) = \int_0^{\infty} \frac{\xi^j d\xi}{1 + e^{(\xi - \mu)}} \quad (4)$$

$$m^* = \frac{h^2}{2k_B T}\left[\frac{n}{4\pi F_{1/2}(\mu)}\right]^{2/3} \quad (5)$$

Note that the effective carrier masses were also computed with a scattering parameter $\lambda = ½$ (to diminish the acoustic phonon-carrier scattering). Values somewhat decrease, but the trend observed with $\lambda = 0$ remains (see Table S2, SI). Transport properties were computed using a semi-classical approach. The electronic transport coefficients for $CuMSnS_4$ (M = V, Co, Ti, Cr) were calculated using the Boltzmann Transport Equation (BTE) and the constant scattering time and the rigid band structure approximation,[64,65] as implemented in the BoltzTrap-1.2.5 code.[66] 5000 k-points were used in the BZ to compute the band derivatives for the transport calculations.

3. Results & Discussion

3.1 Structural and microstructural properties

The room temperature X-ray powder diffraction (XRD) patterns of the SPS processed thiospinel $CuM_{1+x}Sn_{1-x}S_4$ (M = Co, Ti, Cr) compounds are displayed in Figure 2a. The major diffraction peaks can be attributed to the thiospinel structure that was described above (Figure 1), and few noticeable low-intensity peaks were also observed. The very low intensities attested to a small amount of the secondary phase and made it difficult to attribute these to a specific sub-phase. Only the low-intensity peak observed systematically at $2\theta = 26.5°$ can be assigned to the residual graphite of the SPS process (some residual graphite paper particle might have stayed even after the polishing). The Rietveld refinement of the samples M = Ti, Cr, Co converged, and the obtained agreement/reliability factors (Table 1) for the majority of the samples attested to the homogeneity in the composition ranges that were investigated. An illustrative refinement pattern is presented in Figure 2b. For the Ti series, the reliability factors were found to be higher in the case of x = -0.1 and +0.1, due to the slight anisotropic peak broadening arising due to the presence of some possible defects and/or heterogeneous grain morphology. Indeed, it is recently reported that the Ti-based thiospinel can tend to have a Cu off-stoichiometry.[31] This feature presents scope for further investigation at a later stage. Rietveld parameters and refined patterns for all the samples are provided in the SI (Table S1 and Figures S1-S3). The mixed occupancy of the octahedral site can be followed through the evolution of the lattice parameter, a (Table 1). This lattice parameter increases systematically with the Sn-content, which is expected given the differences in the ionic radii of transition

metals, *r* (assuming the oxidation state of +III for Ti and Cr, and +IV for Sn, their corresponding *r* value would be 0.670 Å, 0.615 Å, and 0.690 Å, respectively). Moreover, for Ti and Cr compositions, the mixed occupancy refinement of the octahedral site seems to be consistent with this lattice parameter trend with Sn content. The density of the sintered samples was found to be > 94% of the theoretical density.

Though homogeneous compounds were obtained for the Co, Ti, and Cr-series, the V series was found to be quite challenging (to produce a pure thiospinel phase) by this optimized synthesis methodology. $CuV_{1+x}Sn_{1-x}S_4$ compounds contained a large proportion of the secondary phase (Figure S4a, SI). The pure phase was obtained only for the Sn-rich $CuV_{0.85}Sn_{1.15}S_4$ (x = -0.15) composition in the V series. In any case, the thermoelectric properties, especially the Seebeck coefficients, were found to be quite poor for the V series (Figure S4b, SI). A large number of stable oxidation states for V (2+, 3+, 4+, 5+) might have made propitious the formation of several thermodynamically stable secondary phases, which we could not avoid with our synthesis method. Owing to their abysmal transport properties, the TE results of the V series were not discussed any further. However, their electronic band structures are given in this paper for comparison.

The microstructures at the fractured surface of the sintered $CuM_{1+x}Sn_{1-x}S_4$ (M = Ti, Cr, Co) thiospinel compounds are depicted in Figure 3. The microstructure of the $CuCo_{0.5}Sn_{1.5}S_4$ and $CuTi_{1.1}Sn_{0.9}S_4$ compounds (Figures 3a and 3b) revealed an apparent bimodal distribution of grain size, typically representative of abnormal grain growth. A large number of finely sized grains (< 5 μm) and a considerable proportion of coarse grains (10 – 25 μm) can be observed. The chemical composition of large and small grains were found to be identical. At the outset, the microstructure of the $CuTi_{1.1}Sn_{0.9}S_4$ compound (Figure 3b) does have a larger proportion of equiaxed[67] finer grains (1 - 2 μm). The presence of the abnormal grain growth gives evidence of high local rates of interface migration during the sintering process and potential liquid phase formation at the grain boundaries.[68–70] In the present study, the long step during SPS (30 min) can be a factor for promoting grain growth. The relatively poor mechanical properties observed in these samples can be attributed to the hardness reduction induced by a decrease of the Hall–Petch strengthening.[71,72] The microstructure of the $CuCr_{1.2}Sn_{0.8}S_4$ compound (Figure 3c) looks quite different compared to that of the Co and Ti series and closely resembles that of transgranular failure with noticeable micro-pores existing throughout the fractured surface. This specific microstructure is also the origin of quite poor mechanical properties of the samples.

3.2 Magnetic Properties

The inverse magnetic susceptibility, χ^{-1}, of the compounds $CuCr_{1.2}Sn_{0.8}S_4$ and $CuCo_{0.5}Sn_{1.5}S_4$ was fitted in the temperature region of 100 – 300 K and 150 – 300 K, respectively, using the modified Curie-Weiss law,

$$\chi = \frac{C}{T - \theta} + \chi_0 \qquad (6)$$

with C, θ, and χ_0 are the Curie constant, the Curie-Weiss temperature, and the temperature-independent magnetic susceptibility, respectively. The temperature-independent magnetic susceptibilities were determined through the curve fittings. The magnetic susceptibility of $CuCr_{1.2}Sn_{0.8}S_4$ (Figure 4a) follows the Curie-Weiss behavior in the high-temperature region but deviates below 100 K due to competing ferromagnetic and antiferromagnetic interactions caused by geometric frustration showing a pronounced peak in the ZFC curve at T_{cusp} ~19 K, indicative of a spin-glass transition.[35,73] The effective magnetic

moment μ_{eff} = 3.97 μ_B per Cr atom obtained from the fitting of the high-temperature region is close to the theoretical value μ_{eff} = 3.87 μ_B for octahedral coordination of Cr^{3+} with S = 3/2 and an electronic configuration of t_{2g}^3 (d^3 configuration), which is consistent with a previous report.[39] The temperature dependence of the magnetic susceptibility of $CuCo_{0.5}Sn_{1.5}S_4$ is shown in Figure 4b. The material itself appears to be close to be paramagnetic. An increase in the magnetic susceptibility can be attributed to ferromagnetic impurities of most likely CoS_2 with a Curie temperature T_C = 122 K which agrees well with the observed transition.[74,75] The measurement has been made at high field (H = 50 kOe) in order to saturate this impurity phase possessing strong magnetic behavior. The material shows paramagnetic behavior in the high-temperature region above ~150 K with a Curie-Weiss temperature θ = 11.7 K derived from the fit of the inverse magnetic susceptibility. The effective magnetic moment obtained from the Curie-Weiss fitting is μ_{eff} = 2.93 μ_B per Co atom. The theoretical values (spin only) for octahedrally coordinated Co^{2+} is μ_{eff} = 3.87 μ_B for the high-spin configuration t_{2g}^5 e_g^2 (S = 3/2) and μ_{eff} = 1.73 μ_B for the low-spin configuration $t_{2g}^6e_g^1$ (S = 1/2). Co^{3+} has no unpaired electrons in the low-spin configuration t_{2g}^6 (S = 0) and, therefore, no net magnetic moment. The theoretical effective magnetic moment of Co^{3+} in the high-spin configuration $t_{2g}^4e_g^2$ (S = 2) is μ_{eff} = 4.90 μ_B. The experimentally derived value is comparable to Co^{2+} in the high-spin configuration. However, in the past, the existence of both Co^{2+} and Co^{3+} has been observed by XPS in the related compound $CuCo_2S_4$.[32] The temperature dependence of the magnetic susceptibility and the effective magnetic moment could indicate ferromagnetic ordering due to the existence of both Co (2+) and Co (3+). Such CoS_2 impurity phases are more sensitive under a magnetic field at low temperature and are hard to be detected from room-temperature X-ray diffraction if they are in tiny proportion, say less than 1 wt.%. Therefore, additional investigations need to be realized to resolve this question unambiguously and to correlate it to the thermoelectric properties at low-temperature range. The magnetic susceptibility of $CuTi_{1.1}Sn_{0.9}S_4$ (Figure 4c) shows low values, which are almost independent of the temperature, indicative of Pauli paramagnetism originating from delocalized conduction of electrons, which is corroborated in the forthcoming section with the half-metallic character evidenced in the electrical resistivity of the material.

3.3 TE transport properties

The TE transport properties of $CuCo_{0.5}Sn_{1.5}S_4$ compound are presented in Figure 5. The electrical conductivity, σ, which increases almost linearly with temperature (Figure 5a), varies within ~0.2 x 10^3 S/m at 323 K to ~0.75 x 10^3 S/m at 673 K and is much lower than other Cu-based thiospinels such as Cr-Sb and Co-Ti based compounds.[29–31] The negative Seebeck coefficient, S (Figure 5b), confirms the *n*-type charge transport in the system, *i.e.*, electrons as predominant charge carriers. Careful consideration of the specific charge balance in this Cu-Co-Sn thiospinel compound is required to understand its structural and transport properties. As described in the introduction, the expected charge balance of the Co based compound could be described as $Cu^+Co_{0.5}^{2+}Sn_{1.5}^{4+}(S^{2-})_4$. This is consistent with the magnetic results described in the previous section, where Co seems most probably to sustain its 2+ oxidation state. The electrical transport properties are consistent with this theoretical charge balance and the absence of Cu^{2+} formation, which otherwise will induce the formation of holes and *p*-type conduction. The absolute Seebeck coefficient, $|S|$ marginally increases with temperature from 323 to 673 K, ranging between ~170 μV/K to ~195 μV/K. Based on the tendencies of σ and S, $CuCo_{0.5}Sn_{1.5}S_4$ compound is found to have a semiconducting behavior. The $CuCo_{0.5}Sn_{1.5}S_4$ thiospinel compound with such temperature-dependent tendencies for σ and $|S|$ (and their poor σ values), is close to that of two-dimensional (2D) Mott's variable

range hopping (VRH) systems such as disordered anisotropic materials.[35,76–80] Though the values of *S* are considerable, relatively low σ has resulted in lower power factor ($PF = S^2\sigma$) in this $CuCo_{0.5}Sn_{1.5}S_4$ compound, as shown in Figure 5c. *PF* increases with temperature to reach ~0.3 x 10^{-4} W/m.K^2 at 673 K, but it is almost an order of magnitude lower than other such similar *n*-type thiospinel compounds like $CuTi_2S_4$.[30,31] The $CuCo_{0.5}Sn_{1.5}S_4$ compound exhibited intrinsic low thermal conductivity, κ and it remained almost constant with temperature from 323 to 673 K, ranging around ~1.0 W/m.K, as portrayed in Figure 5d. The majority of the contribution to the total thermal conductivity comes from the lattice phonons ($\kappa \simeq \kappa_{latt}$), as the electronic contribution, κ_e, is almost negligible due to its low σ. The contribution of the localized-vibrations hopping can also affect κ.[81] The large mass difference between Sn and Co can induce a mass fluctuation effect, which suppresses the thermal transport, as reported in several sulfide-based materials such as TiS_2.[46,47] The beneficial effects of lower κ has however been negated by the poor *PF*, thus resulting in a mediocre figure of merit, *zT* (Figure 5e). Nevertheless, the zT_{max} value of ~0.02 at 673 K for this $CuCo_{0.5}Sn_{1.5}S_4$ compound is still slightly higher than that of some similar *n*-type thiospinel compounds that were reported earlier, such as *c*-$CuTi_2S_4$ and $CuCrTiS_4$.[31,76]

The TE transport properties of $CuTi_{1+x}Sn_{1-x}S_4$ (x = 0, 0.1) compounds are presented in Figure 6. For x = -0.1, the sample was found to be quite brittle (as described in the earlier section – Figure 3b), and it broke either after SPS processing or during the cutting and polishing step. Hence, only the thermoelectric properties of compounds with x = 0 and 0.1 are discussed here. The electrical conductivity, σ, decreased monotonically with temperature (Figure 6a). This suggests a metallic/half-metallic behavior, in agreement with band structure calculations that are described in the later section. Increasing the Ti content in $CuTi_{1+x}Sn_{1-x}S_4$ raises σ, which varied between ~70 x 10^3 S/m at 323 K to ~60 x 10^3 S/m at 673 K for the $CuTiSnS_4$ composition, while it is higher for the $CuTi_{1.1}Sn_{0.9}S_4$ composition, varying between ~80 x 10^3 S/m at 323 K to ~65 x 10^3 S/m at 673 K. When compared to that of $CuCo_{0.5}Sn_{1.5}S_4$ compound, σ values of this Ti series are two orders of magnitude higher. The negative Seebeck coefficient, *S* (Figure 6b), confirms the *n*-type charge transport in the Ti series, *i.e.*, electrons as predominant charge carriers. As described above (*i.e.,* introduction), for most of the transition metals, the stable tetravalent state of Sn renders the quaternary thiospinel charge-balanced, *i.e.*, $Cu^+Ti^{3+}Sn^{4+}(S^{2-})_4$ for x = 0. For x > 0, the formation of Ti^{4+} is favorable[30] and conducts to the charge balance as $Cu^+(Ti^{3+})(Ti^{4+})_x(Sn^{4+})_{1-x}(S^{2-})_4$. The electrical conductivity is significantly influenced by the Ti content. DFT calculations, shown in the later section, predicts that Ti orbitals contribute more to the DOS in these compounds (Figure 8a), and for x > 0 (*i.e.*, more Ti content), due to the extension of this conductive Ti/S network, the electron mobility (and thus σ) will be enhanced. This fact is further supported by the shorter bonding distances between the S atoms and the octahedrally coordinated M atoms (d_{M-S} = 2.4720 Å for x = 0.1 and d_{M-S} = 2.4976 Å for x = 0). These factors can explain why with the raise in Ti content, σ was improved. However, the variation in Ti/Sn content (x = 0 or 0.1) did not influence much the *S* values, as both those compositions exhibited roughly the same *S* values throughout the whole temperature range. With Sn not contributing much, the formation of Ti^{4+} (*i.e.*, $3d^0$ electronic configuration) for x > 0, do not induce any significant variation in the carrier concentration, thus resulting in a comparable *S*-values between the $CuTiSnS_4$ (x = 0) and $CuTi_{1.1}Sn_{0.9}S_4$ (x = 0.1) thiospinel compounds. The absolute Seebeck coefficient, $|S|$, increases with temperature, ranging between ~ -30 μV/K at 323 K to ~ -52 μV/K at 673 K. The vastly enhanced σ and considerably lower *S* values have resulted in moderate *PF* values, ranging between 0.16 – 0.18 mW/m.K^2 at 673 K for these $CuTi_{1+x}Sn_{1-x}S_4$ (x = 0, 0.1) compounds (Figure 6c). These values of *PF* for the Ti series,

which increases with temperature, are notably an order of magnitude higher than those of the $CuCo_{0.5}Sn_{1.5}S_4$ compound and comparable with that of similar *n*-type thiospinels such as $CuTi_2S_4$.[30,31] The lattice thermal conductivity, κ_{latt}, for this Ti series (x = 0, 0.1) was found to be appreciably lower, ranging between ~1.4 W/m.K at 323 K to ~0.9 W/m.K at 673 K. The heterogeneous grain morphology (Figure 3b) with the presence of pockets of small grain regions (equiaxed grains)[67] throughout the microstructure of the $CuTi_{1+x}Sn_{1-x}S_4$ compound, as described in the earlier sections with XRD (resulting in slightly higher values of reliability factors during the structural refinement) and SEM results, justifies its low phononic contribution to the thermal conductivity. Notwithstanding the lower κ_{latt}, the thermal conductivity, κ, was not significantly suppressed due to the large contribution coming from the κ_e part (arising from higher σ). κ reaches a minimum of ~1.9 W/m.K and ~1.65 W/m.K at 673 K for x = 0 and 0.1 compositions, respectively. These values of κ coupled with the moderate values of *PF* has made the *n*-type $CuTi_{1+x}Sn_{1-x}S_4$ (x = 0, 0.1) compounds to exhibit modest zT_{max} ~ 0.07 at 673 K, a touch higher than the $CuCo_{0.5}Sn_{1.5}S_4$ compound.

The TE transport properties of $CuCr_{1+x}Sn_{1-x}S_4$ (x = 0.1, 0.2) compounds are presented in Figure 7. The $CuCrSnS_4$ (*i.e.*, x = 0) compound exhibited very low σ and was found to be impossible to be measured (*i.e.*, it was outside the operating limits of our ZEM-2 apparatus); hence it is not presented here. Increasing the Cr content in $CuCr_{1+x}Sn_{1-x}S_4$ (from x = 0.1 to 0.2) emphatically increases σ (Figure 7a). σ also progressively increases with temperature for both the compositions (x = 0.1, 0.2), suggesting a semiconducting behavior, consistent with the band structure computations that are described in the later section. σ reaches a maximum of ~1 x 10^3 S/m at 673 K for the $CuCr_{1.1}Sn_{0.9}S_4$ compound, while ~4.7 x 10^3 S/m at 673 K for $CuCr_{1.2}Sn_{0.8}S_4$ compound. This increasing σ trend with Cr content could be attributed to the rise in charge carrier density. σ for this Cr series is found to be intermediate, *i.e.*, an order of magnitude higher than the Co series and an order of magnitude lower than the Ti series. Unlike the Co and Ti series, the Cr series possesses positive *S* (Figure 7b), confirming the *p*-type charge transport in the system, *i.e.*, holes as predominant charge carriers. In the same way as that of Cu-Ti-Sn thiospinel, the charge balance for x = 0 can be described $Cu^+Cr^{3+}Sn^{4+}(S^{2-})_4$ and a global charge balance of $Cu^+Cr^{3+}(Cr^{4+})_x(Sn^{4+})_{1-x}(S^{2-})_4$.[39,40] for composition $x > 0$. The octahedral occupancy by Cr^{3+} is responsible for the *p*-type conduction. The inception of the re-entrant spin-glass feature for these compounds, as indicated by the magnetic data shown in the previous section, can be correlated to the underlying Cr^{3+} – Cr^{4+} double exchange ferromagnetism,[35,77] that could be favored as the applied external magnetic field can tend to align the ferromagnetic neighboring Cr cation spins in $CuCr_{1+x}Sn_{1-x}S_4$, especially when $x > 0$. The Cr^{4+} ion signaled the formation of a hole in the matrix and raised the carrier concentration for the composition $x > 0$. If Cr^{4+} is unlikely, then the missing electron charge is probably a hole associated with sulfur sublattice.[82] Given that the variation in Cr content significantly influences the carrier concentration, the *S* values were also affected proportionately. $CuCr_{1.1}Sn_{0.9}S_4$ compound exhibits high *S* values of ~350 μV/K, and it remains almost constant in the whole temperature range 323 – 673 K, while the $CuCr_{1.2}Sn_{0.8}S_4$ compound exhibits relatively lower *S* values, with a gradual increase from ~210 μV/K at 323 K to ~260 μV/K at 673 K. Comparing the absolute Seebeck coefficients, $|S|$, of all the three series (Co, Ti, Cr), it can be noted that the Cr series exhibits the best thermopower values over the whole temperature range. Though the Co series and Cr series have the same temperature-dependent tendency for σ and $|S|$ (*i.e.*, both σ, $|S|$ increases with T), the Cr series is more interesting, particularly the $CuCr_{1.2}Sn_{0.8}S_4$ composition due to its better electrical transport properties compared to the cobalt compound. There are

not many such cases where both σ and S increase with temperature, as these transport properties are inversely related as per Boltzmann transport equation. Some VRH systems like higher borides show such features,[83–87] where both σ and S increase with T, however such materials are thermoelectrically viable only at higher temperature ranges. The $CuCr_{1.2}Sn_{0.8}S_4$ compound, though it shows similar behavior, is doubtful to be a VRH system due to its superior electrical conductivity. The possible effect of phonon-drag in addition to the electron diffusion of the degenerate electron systems contributing to the improved electrical transport properties, especially in the $CuCr_{1.2}Sn_{0.8}S_4$ compound cannot be ruled out, since phonon-drag effect has been previously observed in some thiospinel compounds.[76,88–90] However, the possibility can only be speculated now, since direct evidence of phonon drag effect such as sharp peaks in $S(T)$ data typically occur only at lower temperature ranges (10 – 300 K), which is beyond the range of our present measurements. On the other hand, the conventional magnon drag contribution to the Seebeck coefficient is likely to be negligible, as the magnetic data for $CuCr_{1.2}Sn_{0.8}S_4$ compound did not indicate any long-range magnetic order. The improved electrical transport properties have yielded high PF (Figure 7c) for this Cr series when compared to the Co and Ti series. The PF value, which increases with temperature, reaches a maximum of ~0.1 x 10^{-3} W/m.K^2 at 673 K for the $CuCr_{1.1}Sn_{0.9}S_4$ compound, while it reaches as high as ~0.35 x 10^{-3} W/m.K^2 at 673 K for the $CuCr_{1.2}Sn_{0.8}S_4$ compound. This is comparable, and in some cases, even better than some of the other reported thiospinels such as $CuTi_2S_4$, $CuCo_2S_4$, $CuCo_xTi_{2-x}S_4$, $CuCrTiS_4$, and other In-based thiospinel compounds.[30–32,88–90] Among the studied materials, the Cr series manifests the highest effective mass, m^* (Table 2). The considerable interaction between the charge carriers and magnetic moments indicated from the magnetic measurements, may have helped in enhancing m^* without extensively affecting the carrier mobility, which explains the reason for high thermopower and reasonable electrical conductivity (thus high-power factor). Such strategies of utilizing magnetic interactions and dilute magnetic semiconductor systems have yielded striking improvements in TE performance in chalcopyrites and various systems.[15,22,25,43,91,92] The $CuCr_{1+x}Sn_{1-x}S_4$ (x = 0.1, 0.2) compounds exhibited low κ (Figure 7d), which decreased with temperature from 323 to 673 K, ranging between 1.35 – 1.1 W/m.K for $CuCr_{1.1}Sn_{0.9}S_4$ and 1.35 – 1.2 W/m.K for $CuCr_{1.2}Sn_{0.8}S_4$. The lattice phonons contribute majorly to the thermal transport in the Cr series ($\kappa_{latt} >> \kappa_e$). The presence of some surface defects and/or micro-porosity, as observed from the SEM images presented in the previous section (Figure 3c), could have also played a role in this suppressed thermal transport.[93] In addition, the intrinsically low κ in such Sn-based thiospinels can arise from the mass fluctuation effect, induced by the large molar mass of Sn (heavy element). The suppressed thermal transport combined with the enhanced electrical transport properties (PF) has helped the Cr series to manifest higher thermoelectric zT (Figure 7e) when compared to the Co and Ti series. In particular, $CuCr_{1.2}Sn_{0.8}S_4$ displayed zT_{max} ~ 0.2 at 673 K, which is quite respectable for this category of thiospinel compounds. Except for the Sb-doped $CuCr_2S_4$ thiospinel, this value of zT_{max} for the Cr compound is on par with some of the best-reported values for thiospinel compounds (both n and p-types).[29–32,88–90] Results were reproducible and fairly reliable during the heating and cooling cycles.

3.4 Electronic density of states and band structures

Density functional theory calculations (DFT) calculations were performed on a series of $CuM_{1-x}Sn_{1+x}S_4$ thiospinel compounds with specific stoichiometries to understand further the electrical transport properties of these thiospinel compounds. To conveniently compare the electronic structures of $CuM_{1-x}Sn_{1+x}S_4$ thiospinel compounds and to model the 'static' substitution of M atoms (M = V, Co, Ti, Cr), the

crystal structures of $CuM_{1+x}Sn_{1-x}S_4$ were described in lower symmetrical space groups than $Fd\bar{3}m$, such as $P\bar{4}m2$ for M = V, Ti, Cr (x = 0) and $P\bar{4}3m$ for M = Co (x = -0.5). The optimized unit cell parameters and relevant distances are displayed in Table 3. The optimized unit cell parameters computed by DFT were found to be marginally larger than the ones obtained from XRD analysis (especially for the case of Co compound). However, this deviation in lattice parameter values between the experimental XRD and theoretical DFT results falls within the admissible range of 1 – 3%. Cu-S contacts were found to be slightly shorter than those obtained from the XRD analysis, except for $CuCo_{0.5}Sn_{1.5}S_4$, where it is larger. Such similar effects of slight but acceptable variation in the crystallographic parameters between XRD and DFT were also observed in other cases of thiospinels such as $CuCrSbS_4$.[29] No noticeable distortions were found in the tetrahedral environment of Cu, but the Sn-S and M-S (M = Co, Ti, Cr, V) octahedral environments are significantly distorted (refer SI – Table S3 and Figure S5), and this might explain the reason for the reduction in thermal conductivity in some of these thiospinel compounds.

Spin moments (orbital moment are usually very weak for 3d transition metal elements) were computed to be in the range of ca. 3 μ_B for both Cr and Co atoms (2.87 and 3.3 μ_B, respectively), and only 0.80 μ_B, and 1.81 μ_B for Ti, and V atoms, respectively. The values or, more specifically, the trend from the calculated magnetic moments seem to be reasonably consistent and comparable with the experimental magnetic data that were discussed above.

The computed spin-polarized total and atom-projected density of states (DOS) of $CuM_{1+x}Sn_{1-x}S_4$ thiospinel compounds are sketched in Figure 8, and their calculated electronic band structures along high symmetry lines in the BZ for spin-up and spin-down bands are shown in Figures 9-12. The DOS (Figure 8a) and the band structure (Figure 9) for the $CuTiSnS_4$ compound predict it to have a half-metallic behavior with metallic spin-up electrons, but with the spin-down bands which show a semiconductor behavior with a gap of ~0.8 eV. The bottom of the spin-up conduction band is strongly titanium in character with d_{z2} and d_{yz} components. It is in agreement with a formal oxidation state of 3+ for Ti and the computed total spin magnetic moment of 0.80 μ_B (close to one unpaired electron) in $CuTiSnS_4$. The top of the valence band is mainly copper in character with d_{xy} and d_{xz} + d_{yz} components. The computed band structure and DOS for $CuTiSnS_4$ agree with the *n*-type half-metallic character proven experimentally (rather large σ and low negative S, as shown in Figure 6). The half-metallic character computed for $CuTiSnS_4$ is in agreement with the slope of σ (Figure 6a). It is noteworthy that, assuming a rigid band model, increasing the Ti content in $CuTi_{1+x}Sn_{1-x}S_4$ should bring the Fermi level in a higher Ti-based peak of DOS (Figure 8a) and consequently should increase σ as experimentally observed for $CuTi_{1.1}Sn_{0.9}S_4$ with respect to $CuTiSnS_4$ (Figure 6a).

For $CuCo_{0.5}Sn_{1.5}S_4$ compound, the DOS (Figure 8b) and band structure (Figure 10) predict it to have a weak conducting behavior. The vicinity of the Fermi level and the band conduction shows a potential *n*-type charge transport mode in this compound. The bottom of the spin-down conduction band and the top of the spin-down valence band are cobalt in character with d_{x2-y2} + d_{xy} components. On the other hand the top of the spin-up valence band is mainly made of Cu 3*d* components. On the other hand the top of the spin-up valence band is mainly made of Cu 3*d* components. This expected weak metallic character is not in full agreement with the rather small electrical conductivity measured experimentally (Figure 5a), which is strongly weaker than that of the half-metallic $CuTiSnS_4$ compound and its slope, and it indicates rather

a semiconductor behavior. This may put into question the stoichiometry $CuCo_{0.5}Sn_{1.5}S_4$ proposed experimentally. Indeed, in addition to x = -0.5 composition, complementary calculations were also performed for this Co series with x = 0.00 and -0.25 (SI – Figure S6). The modulation of the Fermi level position based on the composition (value of x) was observed, modifying somewhat the electrical properties. A half-metallic situation is expected for low values of x. It also confirms that a Co/Sn substitution rate between 0.5 and 0.75, probably nearer to x = -0.5 to have a Fermi level in the vicinity of the band conduction edge, and the Co charge (positive) is estimated to be between 2.00 and 2.66. However, it must be noted that the thiospinel structure seems to be stable experimentally only when x = -0.5 for this $CuCo_{1+x}Sn_{1-x}S_4$ compound.

The DOS (Figure 8c) and band structure (Figure 11) for $CuVSnS_4$ compound predict it to have a very weak half-metallic (almost semiconducting-like) behavior with E_F lying quite close to the valence band in agreement with the *p*-type charge transport mode that was shown experimentally (Figure S4b, SI). An important V character with 3*d* components is observed in the spin-up valence band but not in the corresponding spin-down band, reflecting the computed magnetic moment (1.81 μ_B) of vanadium atoms. Additionally, the both spin-up and spin-down valence bands contain a strong 3*d* copper contribution. The bottom of the spin-up and spin-down conduction bands is vanadium in character with d_{z2} components.

The DOS (Figure 8d) and band structure (Figure 12) for $CuCrSnS_4$ compound predict a semiconducting behavior with a bandgap of ~0.9 eV, in agreement with the slope of σ measured experimentally. The Cr-projected DOS indicates strong participation of Cr in the spin-up valence band but hardly any contribution in the spin-down valence band that is mainly Cu character with 3*d* component. This militates for magnetic Cr^{3+} ions. Finally, the computed band structure and DOS for this $CuCrSnS_4$ compound agree with the *p*-type semiconducting character proven experimentally (large positive S and medium σ, as shown in Figure 7).

The impact of the substitution at the Sn-site with Ti, V, Cr, and Co atoms was also studied, especially on the electronic part of the transport properties, using a semi-classical approach. Computed Seebeck coefficients as a function of the chemical potential (at 300 K and 700 K) for the $CuM_{1-x}Sn_{1+x}S_4$ (x = 0 for M = Ti, V, Cr, and x = -0.5 for M = Co) compounds are presented in Figure 13. Indeed, the best Seebeck coefficient with respect to the optimal chemical potential is found to be displayed by the $CuCrSnS_4$ compound at room temperature and at a higher temperature, which is coherent with the experimental TE results, where the Cr series outperforms in terms of thermopower when compared to its V/Ti/Co congeners. It must, however, be noted that the values of the computed S-values that are presented in Figure 13 are just qualitative, as the acoustic phonon-carrier scattering was the only scattering contribution taken into account (*i.e.*, λ = 0 in equation 3).

4. Conclusion

By a carefully optimized synthesis and processing methodology, including annealing and sintering conditions, homogeneous *n* and *p*-types thiospinel compounds of the composition $CuM_{1-x}Sn_{1+x}S_4$ (M = Ti, V, Cr, Co) were successfully produced and reported for thermoelectrics for the first time. Based on the measurement of magnetic, electrical and thermal transport properties, and the computation of

electronic band structures and density of states using the first-principles (DFT) calculations, it can be summarized as, in this studied family of Cu-Sn based thiospinel compounds $CuM_{1+x}Sn_{1-x}S_4$ (M = Ti, V, Cr, Co), (i) the *p*-type weak half-metallic $CuV_{1+x}Sn_{1-x}S_4$ compounds exhibited the lowest performing thermoelectric properties (very low *zT*); followed by (ii) the *n*-type conducting $CuCo_{1+x}Sn_{1-x}S_4$ compound with suppressed κ and poor *PF* (high *S*, but quite low σ) resulting in a low zT_{max} ~0.02 at 673; (iii) the *n*-type half-metallic and paramagnetic $CuTi_{1+x}Sn_{1-x}S_4$ series with modest *PF* and κ exhibiting an intermediate zT_{max} ~0.07 at 673 K; and finally (iv) the *p*-type semiconducting and ferromagnetic $CuCr_{1+x}Sn_{1-x}S_4$ series with a better trade-off between the *PF* (high *S*, considerable σ) and κ manifesting an enhanced zT_{max} ~0.2 at 673 K.

Based on the combined experimental and theoretical findings, an interesting plethora of factors seems to have contributed to the improved thermoelectric performance in Cr-Sn thiospinel compounds. Factors such as higher effective mass arising due to the synergistic interaction between carriers and magnetic moments, probable effects of phonon-drag and charge carrier diffusion, simultaneous increase of σ and *S* with temperature, facilitated to boost the power factor. Other factors such as the mass fluctuation effect due to the large molar mass of Sn, presence of some surface defects and/or micro-porosity contribute to the lower thermal transport, and thus cumulatively lead to an overall superior thermoelectric property for Cr-Sn thiospinel compounds when compared to the other Sn-based isoelectronic thiospinel counterparts.

Acknowledgments

This work was supported by the Japanese Society for the Promotion of Science *via* JSPS postdoctoral fellowships - PE17748 (C.B) and P19720 (B.S). T.M acknowledges the funding from JSPS KAKENHI 19F19720, JP16H06441, and JST-Mirai JPMJMI19A1. The Namiki foundry of NIMS is also thanked for the usage of the SEM facility. Prof. Régis Gautier (Rennes) is thanked for his constant support.

References

1 L. E. Bell, *Science*, 2008, **321**, 1457–1461.
2 T. Mori and S. Priya, *MRS Bull.*, 2018, **43**, 176–180.
3 Z. Soleimani, S. Zoras, B. Ceranic, S. Shahzad and Y. Cui, *Sustain. Energy Technol. Assess.*, 2020, **37**, 100604.
4 I. Petsagkourakis, K. Tybrandt, X. Crispin, I. Ohkubo, N. Satoh and T. Mori, *Sci. Technol. Adv. Mater.*, 2018, **19**, 836–862.
5 J. Mao, H. Zhu, Z. Ding, Z. Liu, G. A. Gamage, G. Chen and Z. Ren, *Science*, 2019, **365**, 495–498.
6 T. Zhang, Z. Wang, B. Srinivasan, Z. Wang, J. Zhang, K. Li, C. Boussard-Pledel, J. Troles, B. Bureau and L. Wei, *ACS Appl. Mater. Interfaces*, 2019, **11**, 2441–2447.
7 K. Biswas, J. He, I. D. Blum, C.-I. Wu, T. P. Hogan, D. N. Seidman, V. P. Dravid and M. G. Kanatzidis, *Nature*, 2012, **489**, 414–418.
8 G. J. Snyder and E. S. Toberer, *Nat. Mater.*, 2008, **7**, 105–114.
9 L.-D. Zhao, S.-H. Lo, Y. Zhang, H. Sun, G. Tan, C. Uher, C. Wolverton, V. P. Dravid and M. G. Kanatzidis, *Nature*, 2014, **508**, 373–377.
10 J. Shuai, X. J. Tan, Q. Guo, J. T. Xu, A. Gellé, R. Gautier, J.-F. Halet, F. Failamani, J. Jiang and T. Mori, *Mater. Today Phys.*, 2019, **9**, 100094.

11 F.-J. Fan, B. Yu, Y.-X. Wang, Y.-L. Zhu, X.-J. Liu, S.-H. Yu and Z. Ren, *J. Am. Chem. Soc.*, 2011, **133**, 15910–15913.
12 B. Srinivasan, S. L. Tonquesse, A. Gellé, C. Bourgès, L. Monier, I. Ohkubo, J.-F. Halet, D. Berthebaud and T. Mori, *J. Mater. Chem. A*, 2020, **8**, 19805–19821.
13 G. Tan, F. Shi, S. Hao, L.-D. Zhao, H. Chi, X. Zhang, C. Uher, C. Wolverton, V. P. Dravid and M. G. Kanatzidis, *Nat. Commun.*, 2016, **7**, 12167.
14 Y. He, T. Day, T. Zhang, H. Liu, X. Shi, L. Chen and G. J. Snyder, *Adv. Mater.*, 2014, **26**, 3974–3978.
15 R. Ang, A. U. Khan, N. Tsujii, K. Takai, R. Nakamura and T. Mori, *Angew. Chem. Int. Ed.*, 2015, **54**, 12909–12913.
16 R. Lefèvre, D. Berthebaud, M. Y. Mychinko, O. I. Lebedev, T. Mori, F. Gascoin and A. Maignan, *RSC Adv.*, 2016, **6**, 55117–55124.
17 T. Barbier, D. Berthebaud, R. Frésard, O. I. Lebedev, E. Guilmeau, V. Eyert and A. Maignan, *Inorg. Chem. Front.*, 2017, **4**, 424–432.
18 C. Bourgès, Y. Bouyrie, A. R. Supka, R. Al Rahal Al Orabi, P. Lemoine, O. I. Lebedev, M. Ohta, K. Suekuni, V. Nassif, V. Hardy, R. Daou, Y. Miyazaki, M. Fornari and E. Guilmeau, *J. Am. Chem. Soc.*, 2018, **140**, 2186–2195.
19 R.-Z. Zhang, F. Gucci, H. Zhu, K. Chen and M. J. Reece, *Inorg. Chem.*, 2018, **57**, 13027–13033.
20 V. Pavan Kumar, L. Paradis-Fortin, P. Lemoine, V. Caignaert, B. Raveau, B. Malaman, G. Le Caër, S. Cordier and E. Guilmeau, *Inorg. Chem.*, 2017, **56**, 13376–13381.
21 V. Pavan Kumar, T. Barbier, V. Caignaert, B. Raveau, R. Daou, B. Malaman, G. L. Caër, P. Lemoine and E. Guilmeau, *J. Phys. Chem. C*, 2017, **121**, 16454–16461.
22 T. Mori, *Small*, 2017, **13**, 1702013.
23 K. Suekuni, F. S. Kim and T. Takabatake, *J. Appl. Phys.*, 2014, **116**, 063706.
24 C. Bourgès, M. Gilmas, P. Lemoine, N. E. Mordvinova, O. I. Lebedev, E. Hug, V. Nassif, B. Malaman, R. Daou and E. Guilmeau, *J. Mater. Chem. C*, 2016, **4**, 7455–7463.
25 N. Tsujii and T. Mori, *Appl. Phys. Express*, 2013, **6**, 043001.
26 C. Bourgès, R. Al Rahal Al Orabi and Y. Miyazaki, *J. Alloys Compd.*, 2020, **826**, 154240.
27 Z.-H. Ge, L.-D. Zhao, D. Wu, X. Liu, B.-P. Zhang, J.-F. Li and J. He, *Mater. Today*, 2016, **19**, 227–239.
28 R. Chetty, A. Bali, M. H. Naik, G. Rogl, P. Rogl, M. Jain, S. Suwas and R. C. Mallik, *Acta Mater.*, 2015, **100**, 266–274.
29 A. U. Khan, R. A. R. A. Orabi, A. Pakdel, J.-B. Vaney, B. Fontaine, R. Gautier, J.-F. Halet, S. Mitani and T. Mori, *Chem. Mater.*, 2017, **29**, 2988–2996.
30 C. Bourgès, V. Pavan Kumar, H. Nagai, Y. Miyazaki, B. Raveau and E. Guilmeau, *J. Alloys Compd.*, 2019, **781**, 1169–1174.
31 K. Hashikuni, K. Suekuni, H. Usui, R. Chetty, M. Ohta, K. Kuroki, T. Takabatake, K. Watanabe and M. Ohtaki, *Inorg. Chem.*, 2019, **58**, 1425–1432.
32 Y. Lang, L. Pan, C. Chen and Y. Wang, *J. Electron. Mater.*, 2019, **48**, 4179–4187.
33 Q. Guo, J.-B. Vaney, R. Virtudazo, R. Minami, Y. Michiue, Y. Yamabe-Mitarai and T. Mori, *Inorg. Chem.*, 2018, **57**, 5258–5266.
34 Q. Guo, H.-W. Son and T. Mori, *ACS Appl. Energy Mater.*, 2020, **3**, 2096–2102.
35 D. Berthebaud, O. I. Lebedev, A. Maignan and S. Hebert, *J. Appl. Phys.*, 2018, **124**, 063905.
36 V. P. Sachanyuk, A. O. Fedorchuk, I. D. Olekseyuk and O. V. Parasyuk, *Mater. Res. Bull.*, 2007, **42**, 143–148.
37 D. P. Spitzer, *J. Phys. Chem. Solids*, 1970, **31**, 19–40.
38 J. Padiou, D. Bideau and J. P. Troadec, *J. Solid State Chem.*, 1980, **31**, 401–405.
39 P. Valencia-Gálvez, O. Peña, S. Moris and P. Barahona, *J. Chil. Chem. Soc.*, 2019, **64**, 4285–4289.
40 M. M. Ballal and C. Mande, *Solid State Commun.*, 1976, **19**, 325–327.

41 J. Simon, G. Guélou, B. Srinivasan, D. Berthebaud, T. Mori and A. Maignan, *J. Alloys Compd.*, 2020, **819**, 152999.
42 B. Srinivasan, A. Gellé, J.-F. Halet, C. Boussard-Pledel and B. Bureau, *Materials*, 2018, **11**, 2237.
43 F. Ahmed, N. Tsujii and T. Mori, *J. Mater. Chem. A*, 2017, **5**, 7545–7554.
44 F. Ahmed, N. Tsujii and T. Mori, *J. Materiomics*, 2018, **4**, 221–227.
45 B. Srinivasan, D. Berthebaud and T. Mori, *Energies*, 2020, **13**, 643.
46 M. Beaumale, T. Barbier, Y. Bréard, B. Raveau, Y. Kinemuchi, R. Funahashi and E. Guilmeau, *J. Electron. Mater.*, 2014, **43**, 1590–1596.
47 C. Bourgès, T. Barbier, G. Guélou, P. Vaqueiro, A. V. Powell, O. I. Lebedev, N. Barrier, Y. Kinemuchi and E. Guilmeau, *J. Eur. Ceram. Soc.*, 2016, **36**, 1183–1189.
48 J. Rodríguez-Carvajal, *Phys. B Condens. Matter*, 1993, **192**, 55–69.
49 T. Roisnel and J. Rodríguez-Carvajal, in *Materials Science Forum*, 2001, vol. 378–381, pp. 118–123.
50 A. L. Bail, *Powder Diffr.*, 2005, **20**, 316–326.
51 P. Thompson, D. E. Cox and J. B. Hastings, *J. Appl. Crystallogr.*, 1987, **20**, 79–83.
52 H.-S. Kim, Z. M. Gibbs, Y. Tang, H. Wang and G. J. Snyder, *APL Mater.*, 2015, **3**, 041506.
53 G. Kresse and J. Furthmüller, *Phys. Rev. B*, 1996, **54**, 11169–11186.
54 S. L. Dudarev, G. A. Botton, S. Y. Savrasov, C. J. Humphreys and A. P. Sutton, *Phys. Rev. B*, 1998, **57**, 1505–1509.
55 K. Ramasamy, H. Sims, R. K. Gupta, D. Kumar, W. H. Butler and A. Gupta, *Chem. Mater.*, 2013, **25**, 4003–4009.
56 J. P. Perdew, K. Burke and M. Ernzerhof, *Phys. Rev. Lett.*, 1996, **77**, 3865–3868.
57 P. E. Blöchl, *Phys. Rev. B*, 1994, **50**, 17953–17979.
58 H. J. Monkhorst and J. D. Pack, *Phys. Rev. B*, 1976, **13**, 5188–5192.
59 P. Blaha, K. Schwarz, G. Madsen, D. Kvasnicka and J. Luitz, *WIEN2K: An Augmented Plane Wave plus Local Orbitals Program for Calculating Crystal Properties*, Karlheinz Schwarz, Techn. Universität Wien, Austria, Wien, Austria, 2001.
60 K. Schwarz, P. Blaha and G. K. H. Madsen, *Comput. Phys. Commun.*, 2002, **147**, 71–76.
61 F. Tran, P. Blaha and K. Schwarz, *J. Phys. Condens. Matter*, 2007, **19**, 196208.
62 A. F. May, E. S. Toberer, A. Saramat and G. J. Snyder, *Phys. Rev. B*, 2009, **80**, 125205.
63 E. S. Toberer, A. Zevalkink, N. Crisosto and G. J. Snyder, *Adv. Funct. Mater.*, 2010, **20**, 4375–4380.
64 T. J. Scheidemantel, C. Ambrosch-Draxl, T. Thonhauser, J. V. Badding and J. O. Sofo, *Phys. Rev. B*, 2003, **68**, 125210.
65 G. K. H. Madsen, *J. Am. Chem. Soc.*, 2006, **128**, 12140–12146.
66 G. K. H. Madsen and D. J. Singh, *Comput. Phys. Commun.*, 2006, **175**, 67–71.
67 E. Tzimas and A. Zavaliangos, *Mater. Sci. Eng. A*, 2000, **289**, 228–240.
68 F. Gucci, T. G. Saunders, B. Srinivasan, F. Cheviré, D. A. Ferluccio, J.-W. G. Bos and M. J. Reece, *J. Alloys Compd.*, 2020, **837**, 155058.
69 R. Chaim, G. Chevallier, A. Weibel and C. Estournès, *J. Mater. Sci.*, 2018, **53**, 3087–3105.
70 B. Srinivasan, A. Gellé, F. Gucci, C. Boussard-Pledel, B. Fontaine, R. Gautier, J.-F. Halet, M. J. Reece and B. Bureau, *Inorg. Chem. Front.*, 2019, **6**, 63–73.
71 J. R. Weertman, *Mater. Sci. Eng. A*, 1993, **166**, 161–167.
72 N. Hansen, *Scr. Mater.*, 2004, **51**, 801–806.
73 F. Kariya, S. Ebisu and S. Nagata, *J. Solid State Chem.*, 2009, **182**, 608–616.
74 S. Hébert, E. Guilmeau, D. Berthebaud, O. I. Lebedev, V. Roddatis and A. Maignan, *J. Appl. Phys.*, 2013, **114**, 103703.
75 B. Morris, V. Johnson and A. Wold, *J. Phys. Chem. Solids*, 1967, **28**, 1565–1567.
76 M. Ito, T. Yamashita, S. Ebisu and S. Nagata, *J. Alloys Compd.*, 2014, **598**, 133–136.
77 T. Furubayashi, H. Suzuki, N. Kobayashi and S. Nagata, *Solid State Commun.*, 2004, **131**, 505–508.
78 H. Liu, H. S. Choe, Y. Chen, J. Suh, C. Ko, S. Tongay and J. Wu, *Appl. Phys. Lett.*, 2017, **111**, 102101.

79 P. Nagels, M. Rotti and R. Gevers, *J. Non-Cryst. Solids*, 1983, **59–60**, 65–68.
80 S. J. Choi, B.-K. Kim, T.-H. Lee, Y. H. Kim, Z. Li, E. Pop, J.-J. Kim, J. H. Song and M.-H. Bae, *Nano Lett.*, 2016, **16**, 3969–3975.
81 T. Ren, Z. Han, P. Ying, X. Li, X. Li, X. Lin, D. Sarker and J. Cui, *ACS Appl. Mater. Interfaces*, 2019, **11**, 32192–32199.
82 S. Bordács, I. Kézsmárki, K. Ohgushi and Y. Tokura, *New J. Phys.*, 2010, **12**, 053039.
83 T. Mori and T. Nishimura, *J. Solid State Chem.*, 2006, **179**, 2908–2915.
84 T. Mori, *J. Appl. Phys.*, 2005, **97**, 093703.
85 O. A. Golikova, N. Amandzhanov, M. M. Kazanin, G. M. Klimashin and V. V. Kutasov, *Phys. Status Solidi A*, 1990, **121**, 579–586.
86 T. Mori, D. Berthebaud, T. Nishimura, A. Nomura, T. Shishido and K. Nakajima, *Dalton Trans.*, 2010, **39**, 1027–1030.
87 T. Mori, *J. Solid State Chem.*, 2019, **275**, 70–82.
88 P. Wyżga, I. Veremchuk, C. Himcinschi, U. Burkhardt, W. Carrillo-Cabrera, M. Bobnar, C. Hennig, A. Leithe-Jasper, J. Kortus and R. Gumeniuk, *Dalton Trans.*, 2019, **48**, 8350–8360.
89 P. Wyżga, I. Veremchuk, M. Bobnar, P. Koželj, S. Klenner, R. Pöttgen, A. Leithe-Jasper and R. Gumeniuk, *Chem. – Eur. J.*, 2020, **26**, 5245 –5256.
90 P. Wyżga, I. Veremchuk, M. Bobnar, C. Hennig, A. Leithe-Jasper and R. Gumeniuk, *Z. Für Anorg. Allg. Chem.*, 2020, **646**, 1–9.
91 J.-B. Vaney, S. Aminorroaya Yamini, H. Takaki, K. Kobayashi, N. Kobayashi and T. Mori, *Mater. Today Phys.*, 2019, **9**, 100090.
92 N. Tsujii, A. Nishide, J. Hayakawa and T. Mori, *Sci. Adv.*, 2019, **5**, eaat5935.
93 R. V. R. Virtudazo, B. Srinivasan, Q. Guo, R. T. Wu, T. Takei, K. Kuroda, H. Wada, Y. Shimasaki, S. Bernik and T. Mori, *Inorg. Chem. Front.*, 2020. DOI:10.1039/D0QI00888E.

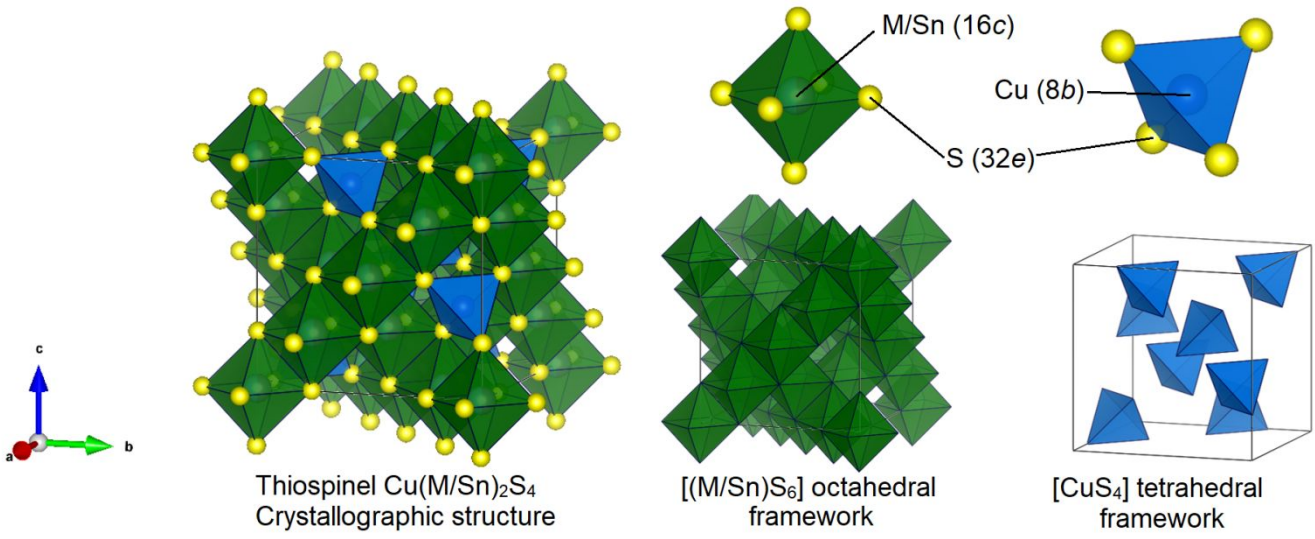

Figure 1. *Standardized crystallographic structure of the* $CuM_{1+x}Sn_{1-x}S_4$ *thiospinel* ($Fd\bar{3}m$) *compound.*

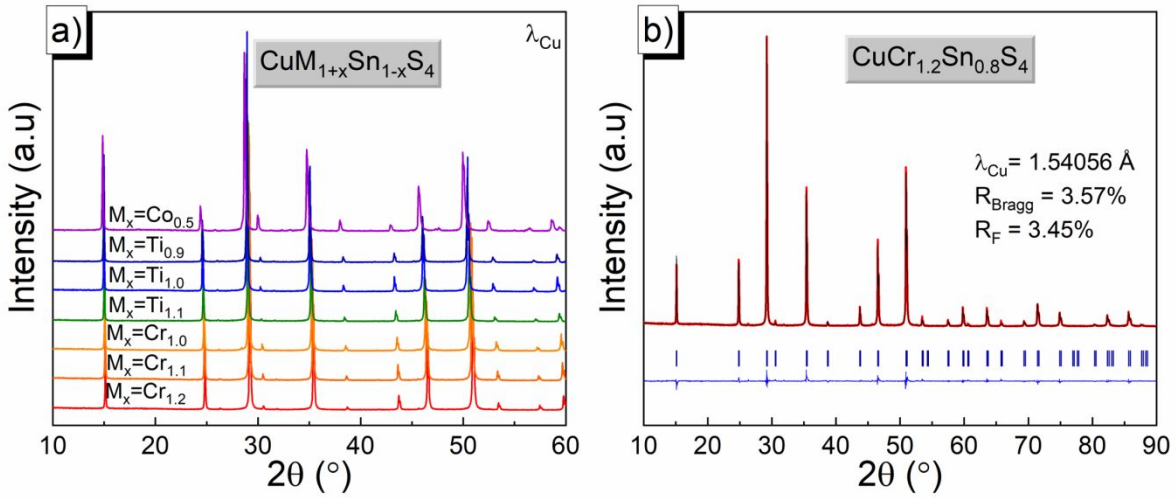

Figure 2. *(a) Room-temperature XRD patterns of the SPS processed $CuM_{1+x}Sn_{1-x}S_4$ (with M = Co, Ti, Cr) thiospinel compounds and (b) an illustrative Rietveld refinement for the $CuCr_{1.2}Sn_{0.8}S_4$ compound.*

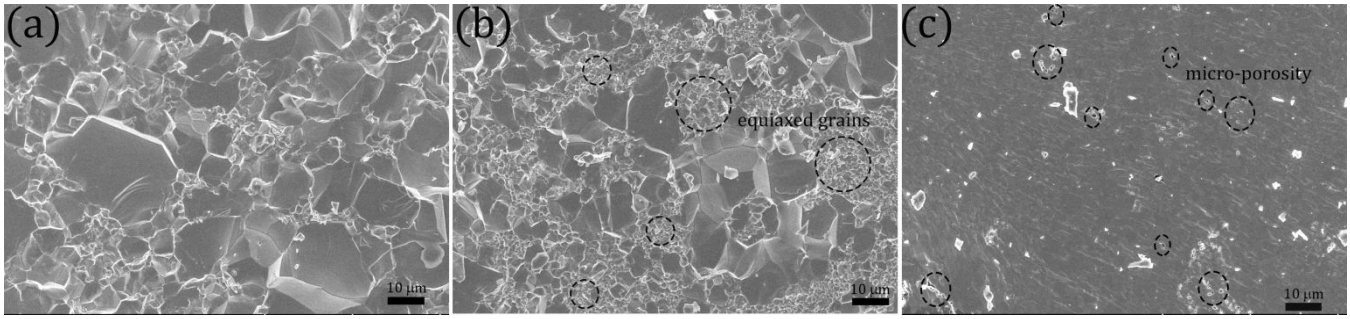

Figure 3. *SEM images showing the microstructure at the fractured surface of the SPS processed (a) $CuCo_{0.5}Sn_{1.5}S_4$, (b) $CuTi_{1.1}Sn_{0.9}S_4$, (c) $CuCr_{1.2}Sn_{0.8}S_4$ thiospinel compounds.*

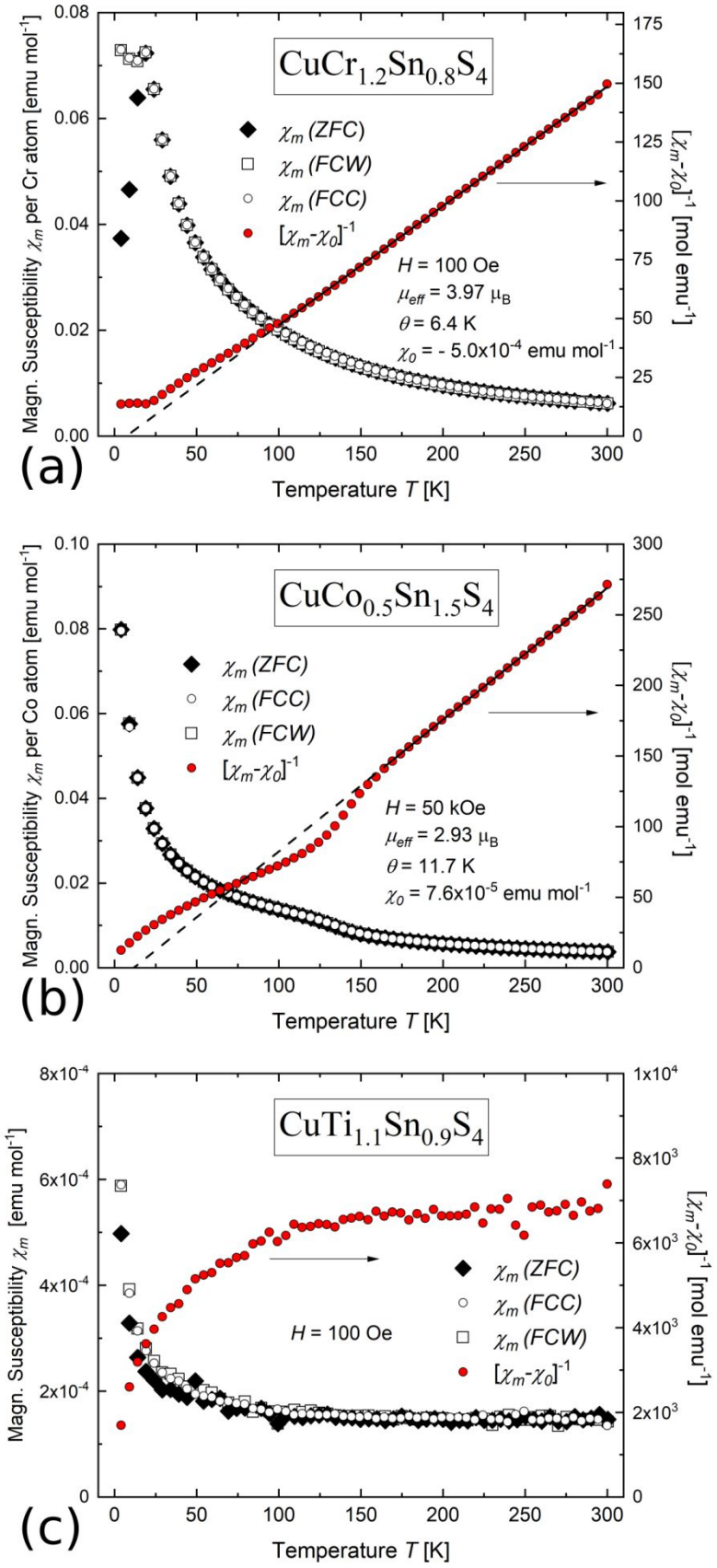

Figure 4. *Temperature-dependent magnetic susceptibility of (a) $CuCr_{1.2}Sn_{0.8}S_4$, (b) $CuCo_{0.5}Sn_{1.5}S_4$, and (c) $CuTi_{1.1}Sn_{0.9}S_4$ thiospinel compounds.*

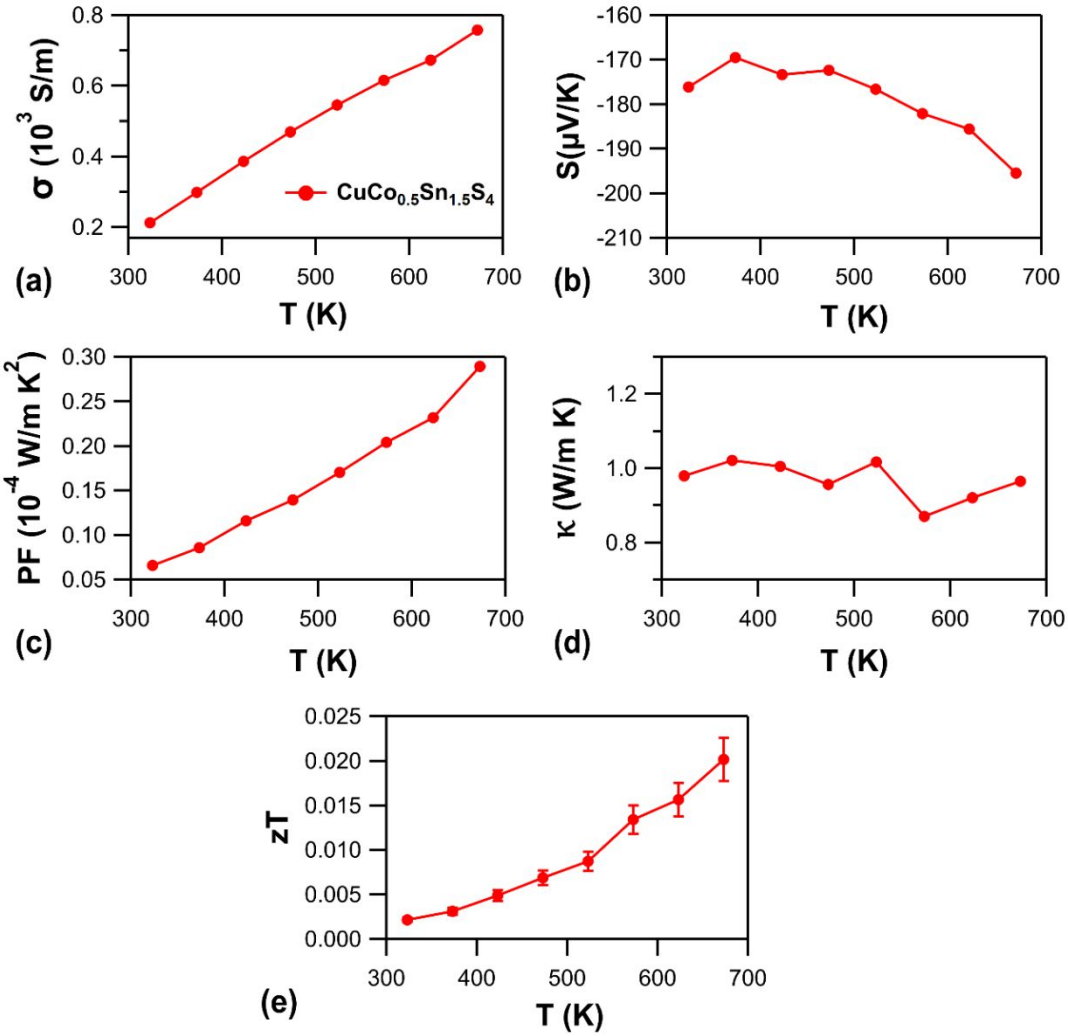

Figure 5. *Temperature-dependent transport properties for* $CuCo_{1+x}Sn_{1-x}S_4$ *(x = –0.5) compound – (a) electrical conductivity, σ, (b) Seebeck coefficient, S, (c) Power factor, PF, (d) Total thermal conductivity, κ, and (e) figure of merit, zT.*

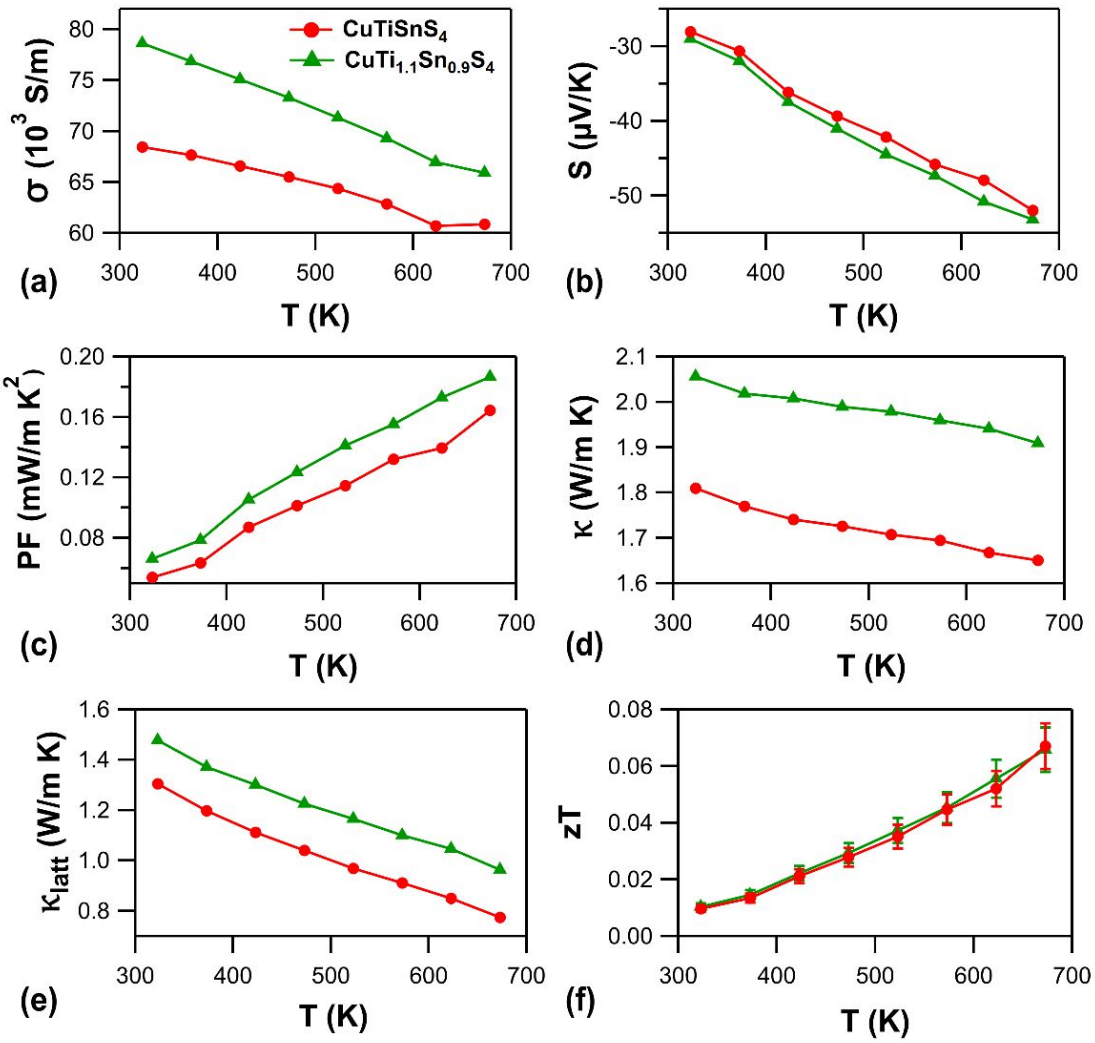

Figure 6. *Temperature-dependent transport properties for* $CuTi_{1+x}Sn_{1-x}S_4$ *(x = 0, 0.1) compounds – (a) electrical conductivity, σ, (b) Seebeck coefficient, S, (c) Power factor, PF, (d) Total thermal conductivity, κ, (e) Lattice thermal conductivity,* κ_{latt}*, and (f) figure of merit, zT.*

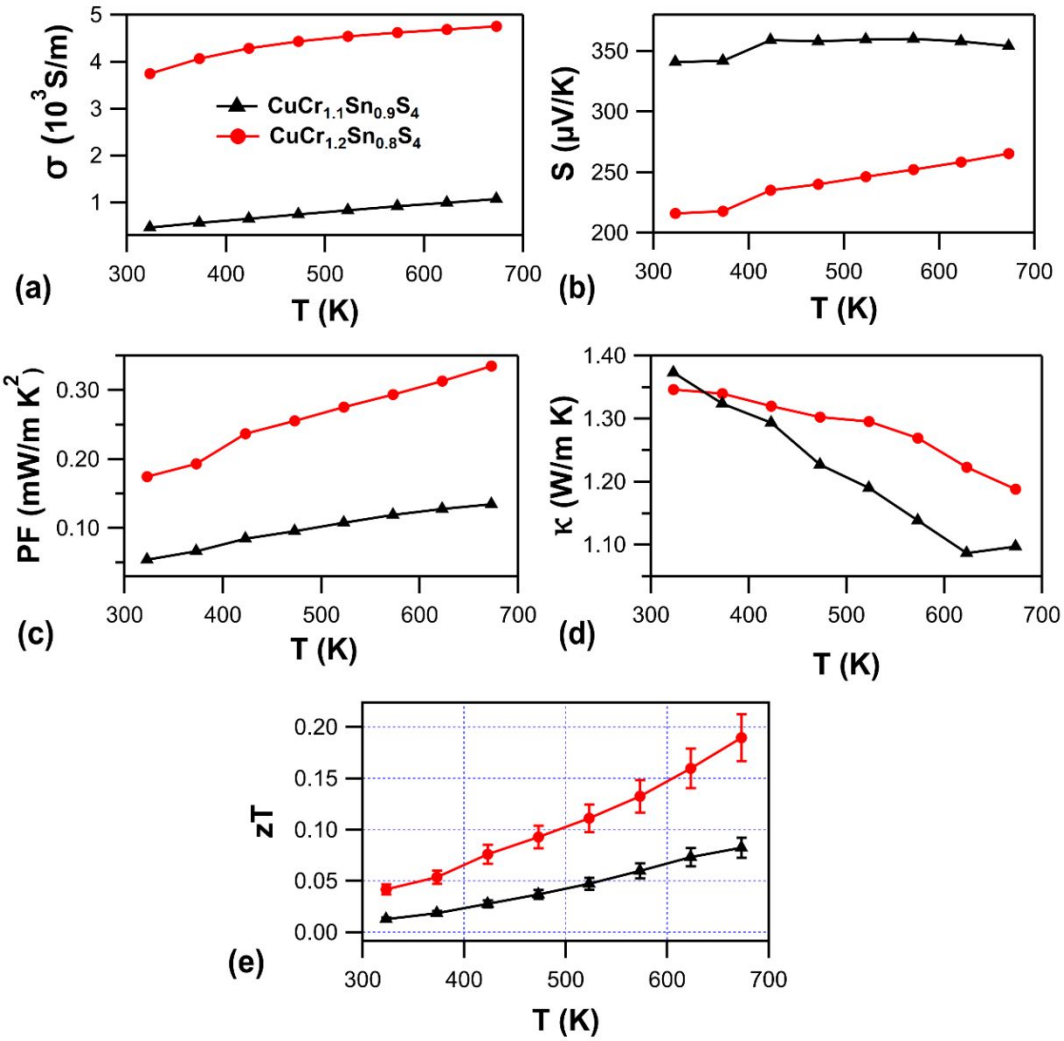

***Figure 7**. Temperature-dependent transport properties for $CuCr_{1+x}Sn_{1-x}S_4$ (x = 0.1, 0.2) compounds – (a) electrical conductivity, σ, (b) Seebeck coefficient, S, (c) Power factor, PF, (d) Total thermal conductivity, κ, and (e) figure of merit, zT.*

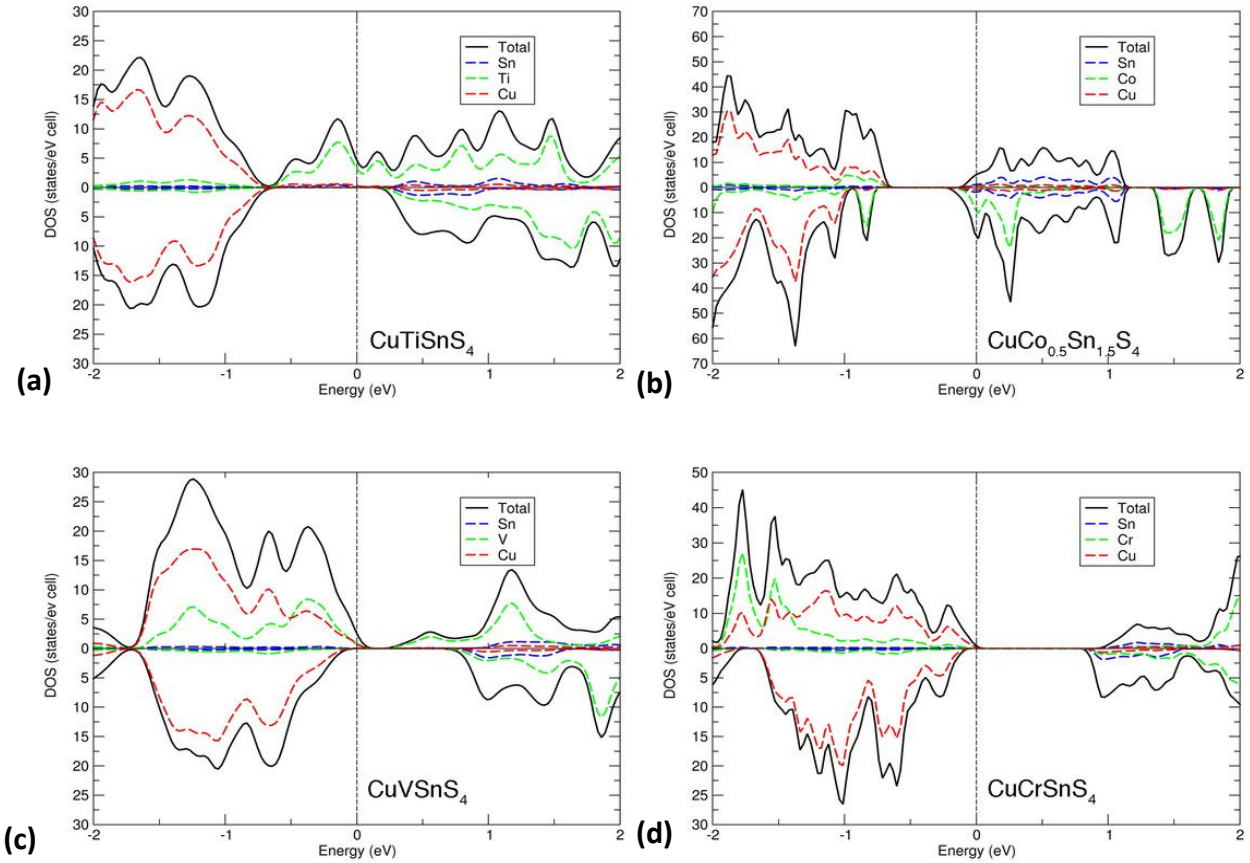

Figure 8. *Total and atom-projected spin-polarized density of states (DOS) of (a) $CuTiSnS_4$, (b) $CuCo_{0.5}Sn_{1.5}S_4$, (c) $CuVSnS_4$, and (d) $CuCrSnS_4$ thiospinel compounds.*

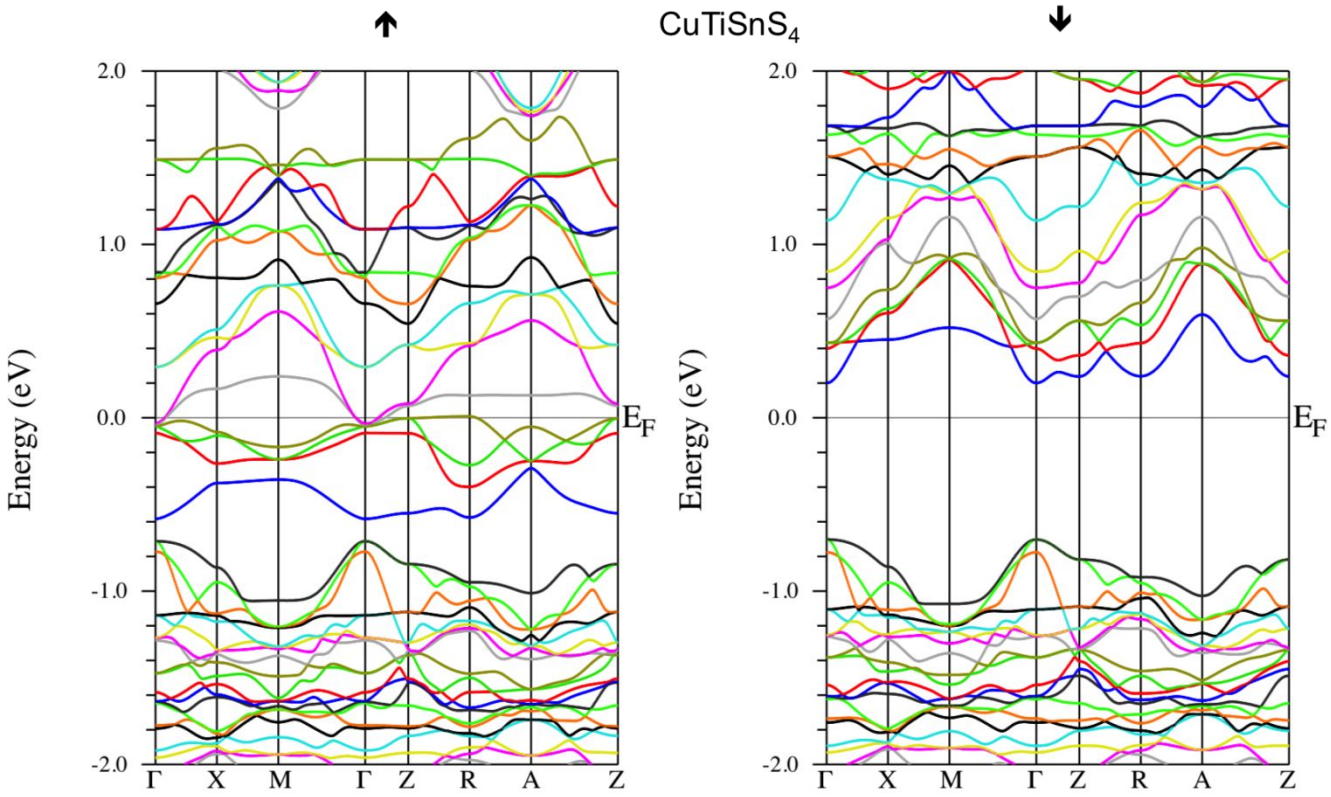

Figure 9. *Spin-polarized band structures for $CuTiSnS_4$ thiospinel compound (spin-up (left) and spin-down (right) channels)*

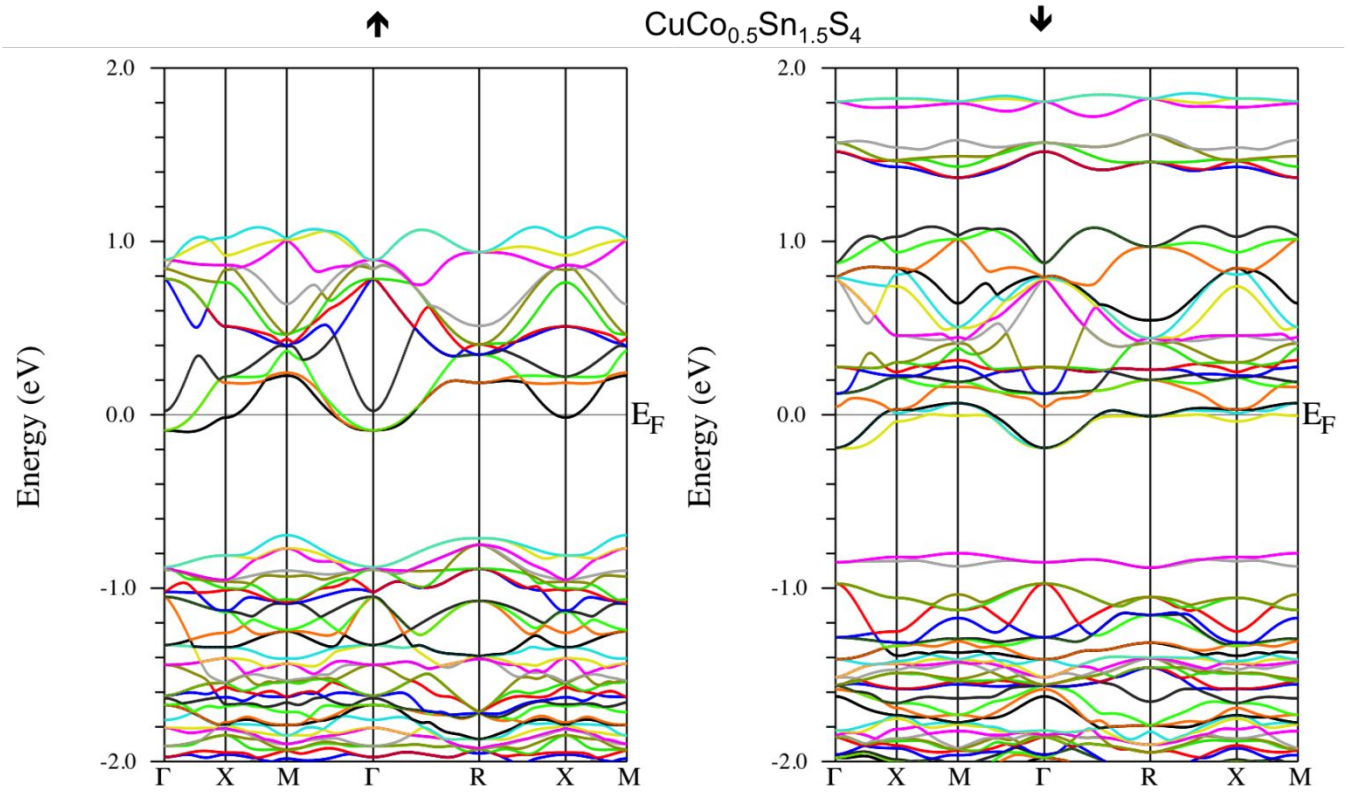

Figure 10. *Spin-polarized band structures for $CuCo_{0.5}Sn_{1.5}S_4$ thiospinel compound (spin-up (left) and spin-down (right) channels)*

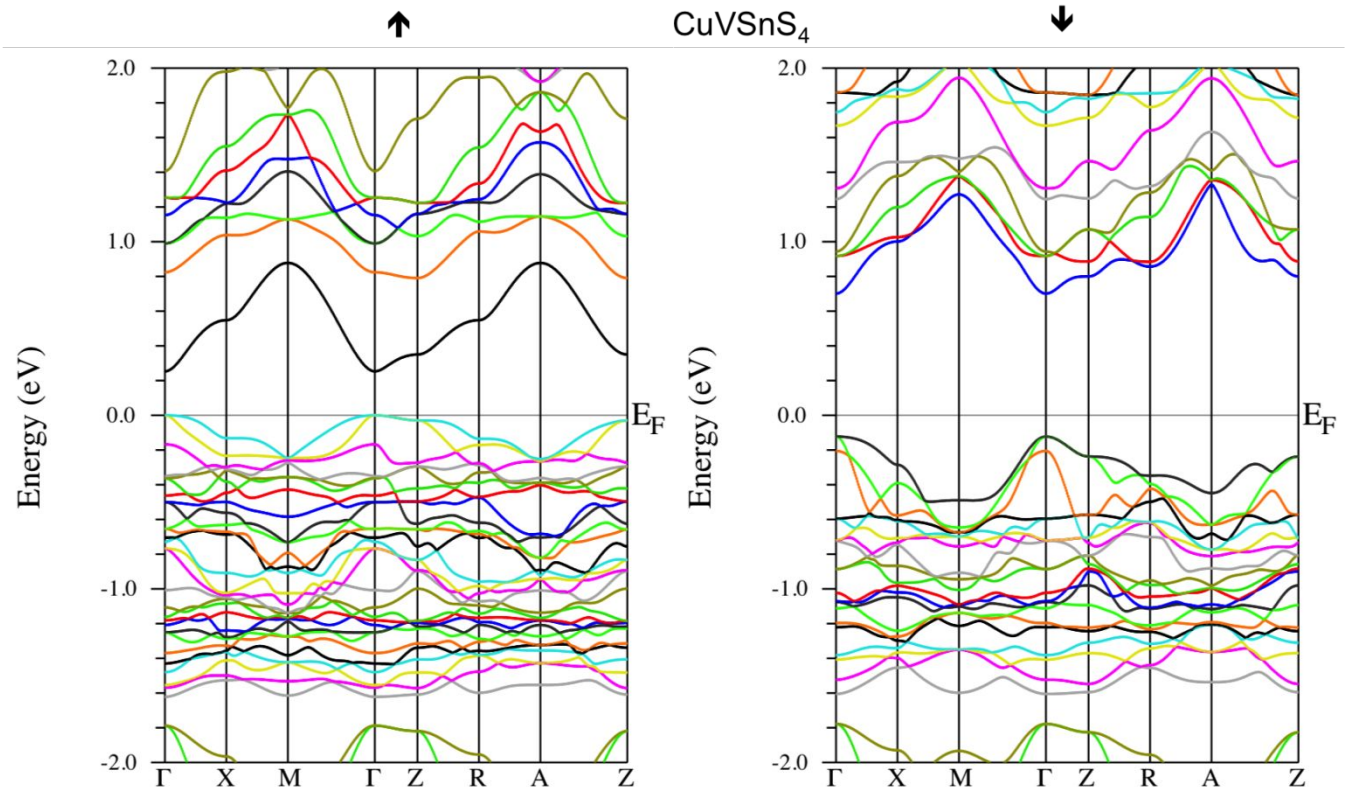

Figure 11. *Spin-polarized band structures for $CuVSnS_4$ thiospinel compound (spin-up (left) and spin-down (right) channels).*

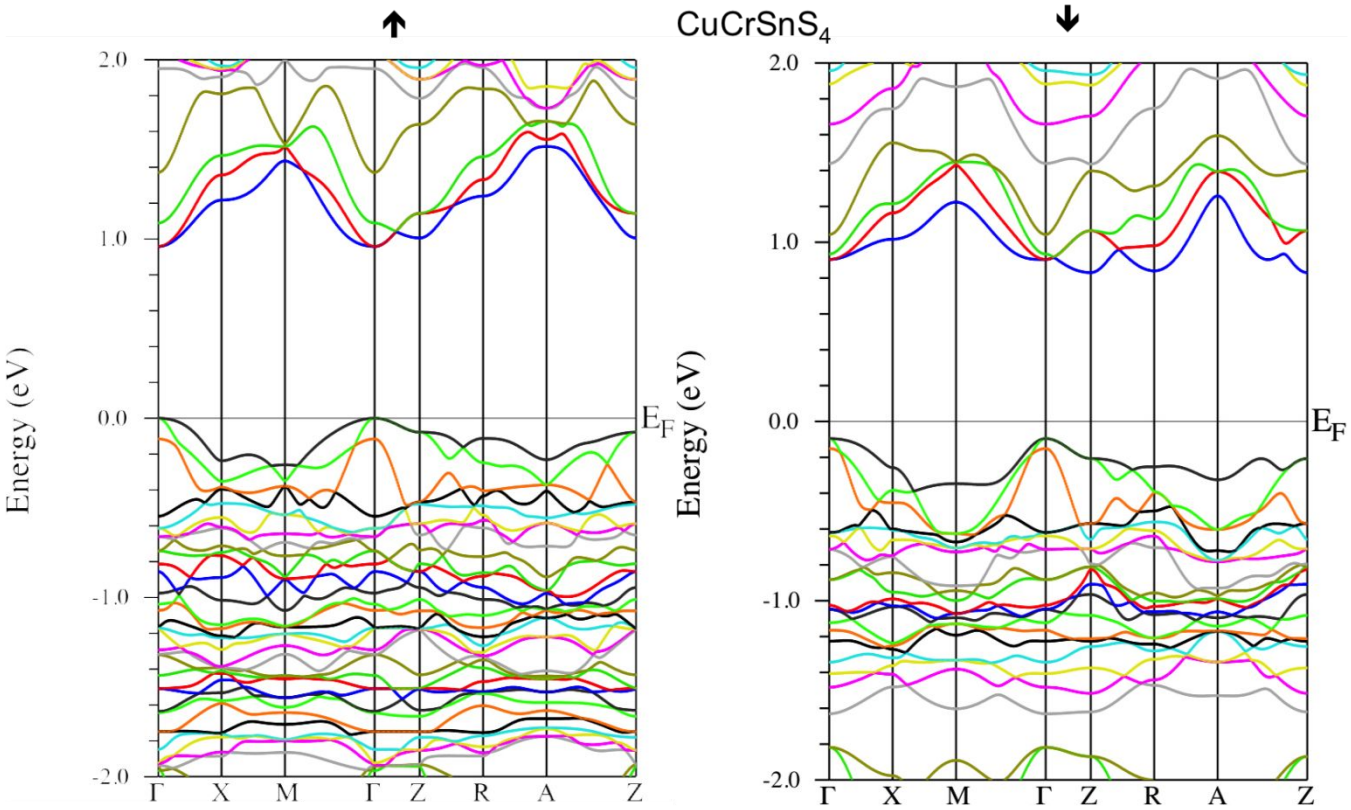

Figure 12. *Spin-polarized band structures for $CuCrSnS_4$ thiospinel compound (spin-up (left) and spin-down (right) channels).*

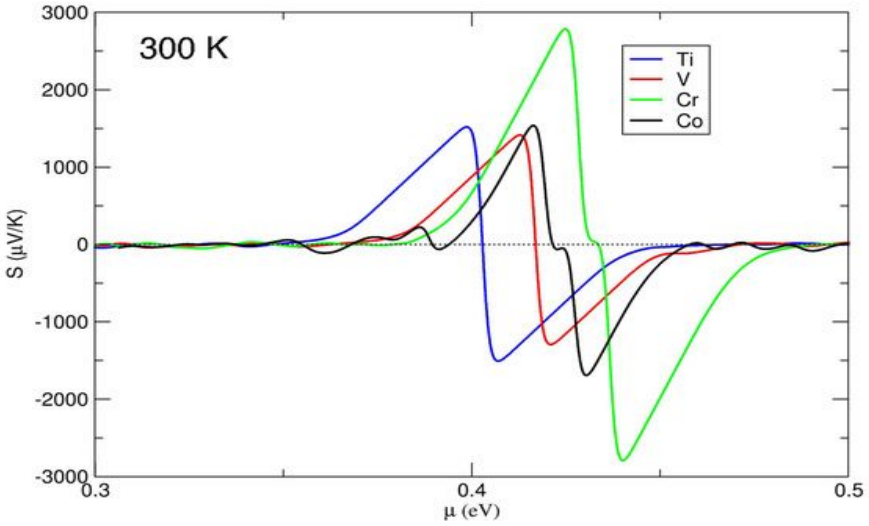

(a)

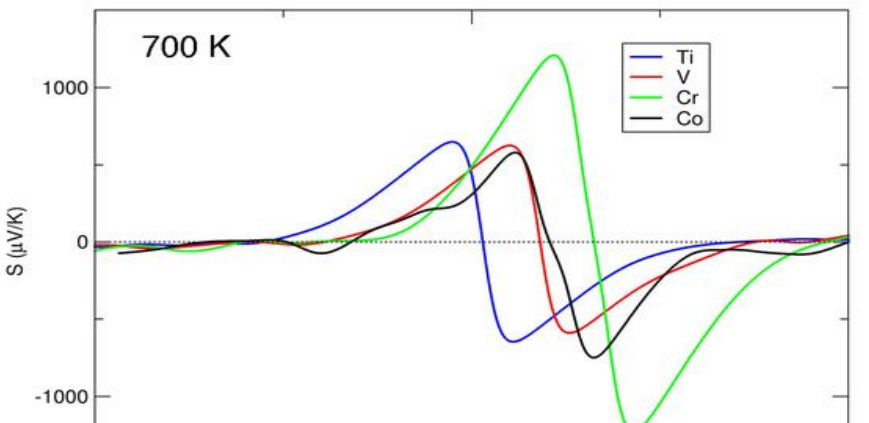

Figure 13. *Computed Seebeck coefficient at T = 300 K (a) and 700 K (b) as a function of the chemical potential for $CuM_{1+x}Sn_{1-x}S_4$ (x= 0 with M = Ti, Cr, V and x = -0.5 with M = Co) thiospinel compounds.*

Table 1. *Cell parameters and reliability factors obtained from Rietveld refinement of XRD patterns (λ_{Cu} = 1.54056 Å) and relative densities of the SPS processed $CuM_{1+x}Sn_{1-x}S_4$ (with M = Co, Ti, Cr) thiospinel compounds.*

$Cu(M;Sn)_2S_4$; $Fd\bar{3}m$; λ_{Cu} = 1.54056 Å; 300 K						
	a (Å)	**V (Å)**	**χ^2**	**R_{Bragg}**	**R_F**	**Relative density (%)**
$CuCo_{0.5}Sn_{1.5}S_4$	10.313(1)	1096.7(1)	4.30	3.90	3.22	97.81
$CuTi_{0.9}Sn_{1.1}S_4$	10.233(1)	1071.5(1)	9.20	12.70	7.74	96.29
$CuTiSnS_4$	10.228(1)	1070.1(1)	4.57	6.93	5.21	96.43
$CuTi_{1.1}Sn_{0.9}S_4$	10.196(1)	1060.0(1)	9.76	13.70	9.11	94.53
$CuCrSnS_4$	10.172(1)	1052.5(1)	2.49	3.95	2.89	96.36
$CuCr_{1.1}Sn_{0.9}S_4$	10.152(1)	1046.3(1)	2.92	4.18	3.02	96.94
$CuCr_{1.2}Sn_{0.8}S_4$	10.133(1)	1040.5(1)	2.56	3.57	3.45	96.93

Table 2. *Computed carrier concentration and effective mass values at room temperature for $CuM_{1+x}Sn_{1-x}S_4$ (x= 0 for M = Ti, Cr, and x = -0.5 for M = Co)[a] and for λ = 0.*

Computed transport properties (based on band structures)	**$CuCo_{0.5}Sn_{1.5}S_4$**	**$CuTiSnS_4$**	**$CuCrSnS_4$**
Carrier concentration, *n* (cm^{-3})	1.6 x 10^{20}	1.9 x 10^{20}	3.3 x 10^{19}
Effective mass, *m**	3.03	0.49	4.68

(m_e)			

[a] The values of carrier concentration (n) were computed from the electronic band structures, and hence their absolute values are higher than what it could result from experimental studies (from Hall measurements, for instance). The tendency of n with M must be considered, rather than their absolute values.

Table 3. *DFT optimized cell parameters and pertinent distances (Å) of* $CuM_{1+x}Sn_{1-x}S_4$ *(x = 0 for M = Ti, V, Cr, and x = -0.5 for M = Co) thiospinel compounds.*

Structural Information	**$CuCo_{0.5}Sn_{1.5}S_4$**	**$CuTiSnS_4$**	**$CuCrSnS_4$**	**$CuVSnS_4$**
a	10.384	7.259	7.229	7.179
b	10.384	7.259	7.229	7.179
c	10.384	10.376	10.252	10.177
Cu-S	2.322	2.320	2.310	2.311
Sn-S	2.583-2.662	2.534-2.609	2.517-2.594	2.535-2.590
M-S (M = Co, Ti, Cr, V)	2.466-2.623	2.511-2.601	2.440-2.567	2.465-2.537

Table of Content (TOC)

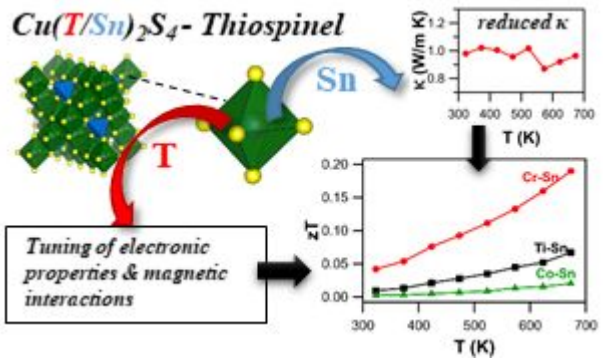

The thermoelectric properties of a series of Cu-Sn based thiospinel compounds by screening a variety of transition elements (M = Ti, V, Cr, Co) as a potential substituent at the Sn-site (both *p*- and *n*-type thiospionels) are reported and commented.